Size-resolved source apportionment of particulate matter in urban Beijing during haze and non-haze episodes

S. L Tian, Y. P. Pan, Y. S. Wang

State Key Laboratory of Atmospheric Boundary Layer Physics and Atmospheric Chemistry (LAPC), Institute of Atmospheric Physics, Chinese Academy of Sciences, Beijing 100029, China

[*]Corresponding author. Tel.: +86 01082020530; fax: +86 01062362389.

E-mail address: wys@mail.iap.ac.cn (Y. Wang); panyuepeng@mail.iap.ac.cn (Y. Pan).

Abstract: Additional size-resolved chemical information is needed before the physicochemical characteristics and sources of airborne particles can be understood; however, this information remains unavailable in most regions of China due to lacking measurement data. In this study, we report observations of various chemical species in size-segregated particle samples that were collected over one year in the urban area of Beijing, a mega city that experiences severe haze episodes. In addition to fine particles, high concentrations of coarse particles were measured during the period of haze. The abundance and chemical compositions of the particles in this study were temporally and spatially variable, with major contributions from organic matter and secondary inorganic aerosols. The contributions of organic matter to the particle mass decreased from 37.9% to 31.2%, and the total contribution of sulfate (SO_4^{2-}), nitrate (NO_3^-) and ammonium (NH_4^+) ions increased from 19.1% to 33.9% between non-haze and haze days, respectively. Due to heterogeneous reactions and hygroscopic growth, the peak size distributions of the organic carbon, copper (Cu) and SO_4^{2-}, NO_3^-, NH_4^+, chloride (Cl^-), and potassium (K^+) ions shifted from 0.43-0.65 μm on non-haze days to 0.65-1.1 μm on haze days. Although the size distributions of lead (Pb), cadmium (Cd) and thallium (Tl) were similar during the observation period, their concentrations increased by a factor of more than 1.5 on haze days compared with non-haze days. We observed that NH_4^+, which has a size range of 0.43-0.65 μm, SO_4^{2-} and NO_3^-, which have a size range of 0.65-1.1 μm, calcium ions (Ca^{2+}), which have a size range of 5.8-9 μm, and the meteorological factors of relative humidity and wind speed were responsible for haze pollution when the visibility was

less than 10 km. Source apportionment using positive matrix factorization showed six PM$_{2.1}$ sources and seven PM$_{2.1-9}$ common sources: secondary inorganic aerosol (25.1% for fine particles vs. 9.8% for coarse particles), coal combustion (17.7% vs. 7.8%), biomass burning (11.1% vs. 11.8%), industrial pollution (12.1% vs. 5.1%), road dust (8.4% vs. 10.9%), vehicle emissions (19.6% for fine particles), mineral dust (22.6% for coarse particles) and organic aerosol (23.6% for coarse particles). The first four factors and vehicle emissions were higher on haze days, while the contributions of road dust and mineral dust were higher on non-haze days. The sources generally increased as the size decreased, with the exception of mineral dust. However, two peaks were consistently found in the fine and coarse particles. In addition, the contributing sources varied with the wind direction, with coal and oil combustion products increasing during southern flows. This result suggests that future air pollution control strategies should consider wind patterns, especially during episodes of haze. Furthermore, the findings of this study indicated that the PM$_{2.5}$-based dataset is insufficient for determining source control policies for haze in China and that detailed size-resolved information is needed to characterize the important sources of particulate matter (PM) in urban regions and better understand severe haze pollution.

Introduction

Particulate matter (PM) is among the most important atmospheric pollutants that negatively affect human health and visibility. In addition, PM plays a significant role in global climate change through its direct and indirect affects and ecosystem cycling (Huang et al., 2014; McFiggans, 2014; Pan et al., 2013). Due to rapid industrialization and urbanization in recent decades, China has become one of the most significant source regions for anthropogenic atmospheric emissions in the world (Guo et al., 2014). The Chinese capital of Beijing, a megacity with approximately 21 million inhabitants (Beijing statistical yearbook 2013), is experiencing extreme haze events

59 (Sun et al., 2006). From November 30 to December 2 and December 7 to December 8,

60 2004, the highest concentration of $PM_{2.5}$ (particulate matter with aerodynamic

61 diameter lower than 2.5 μm) over 6 hours was 329.8 μg m^{-3} (Sun et al., 2006). During

62 the haze episode in January 2013, the highest instantaneous five-minute $PM_{2.5}$

63 concentration was 770 μg m^{-3} at 20:48 on January 12, 2013. Moreover, the highest

64 instantaneous $PM_{2.5}$ concentration reached 1000 μg m^{-3} in some heavily polluted

65 areas of Beijing (Quan et al., 2014). Although previous studies have provided

66 valuable information regarding the physical and chemical characteristics of PM in

67 urban Beijing and its surrounding areas (Li et al., 2013; Du et al., 2014; Song et al.,

68 2006; Chan et al., 2005; Schleicher et al., 2013; Sun et al., 2004), the factors that

69 influence haze formation remain unclear due to its complexity (Yang et al., 2014; Jing

70 et al., 2014). In addition, previous studies have primarily focused on single particle

71 fractions, such as $PM_{2.5}$, and have neglected size-resolved chemical information,

72 especially for coarse particles, which also play an important role in haze events (Tian

73 et al., 2014; Sun et al., 2013).

74   Knowing the size distributions and associated chemical species is crucial for

75 evaluating the effects of PM on human health, visibility, and regional radiative

76 forcing, and for determining the sources, formation mechanisms and conversion

77 processes of the particles (Pillai and Moorthy, 2001; Duarte et al., 2008; Liu et al.,

78 2008; Contini et al., 2014). Typically, mass distribution of PM is dominated by three

79 modes (or sub-modes): the condensation (~0.1- 0.5 μm), droplet (~0.5- 2 μm) and

80 coarse (> 2 μm) modes (Wang et al., 2012; Guo et al., 2010). Thus, to simplify mass

81 distribution calculations in this study, the particle modes were divided. The sizes of

82 the condensation mode particles were between 0.43 and 0.65 μm, and the sizes of the

83 droplet-mode particles were between 0.65 and 2.1 μm. Recent results have suggested

84 that secondary sulfates and nitrates primarily form fine particles, with elevated

85 concentrations in the droplet mode during haze days (Sun et al., 2013; Wang et al.,

86 2012). During the extreme haze events in urban Beijing in early 2013, the peak mass

concentration of particles shifted from 0.43-0.65 μm on clear days to 0.65-1.1 μm on lightly polluted days and 1.1-2.1 μm on heavily polluted days due to the hygroscopic growth of submicron particles and the formation of secondary particles, including organic carbon (OC) and sulfate (SO_4^{2-}), nitrate (NO_3^-) and ammonium (NH_4^+) ions (Tian et al., 2014). Because long-term observations are lacking, it is unclear whether the peak shifts occurred during other periods or whether this phenomenon only occurred during the extreme haze events in early 2013.

In addition, source apportionment based on size-fractionated PM data would provide additional insights regarding aerosol sources, especially during haze events (Pant and Harrison, 2012). For example, receptor models have been successfully used to identify coarse aerosol sources separately of fine aerosol sources (Karanasiou et al., 2009; Titos et al., 2014). Source apportionment studies have shown that the sources of PM_{10} (particulate matter with aerodynamic diameter lower than 10 μm) and $PM_{2.5}$ are different. Meanwhile, the features of sources and dominant sources during different periods are different (Karanasiou et al., 2009; Vecchi et al., 2008), and understanding the sources of size-resolved chemical species (i.e., OC, SO_4^{2-}, NO_3^- and NH_4^+) is important for strategy-makers to effectively control and manage pollution (Hou et al., 2011; Zhang et al., 2014a; Fisher et al., 2011).

The main source apportionment methods can be divided into three categories: emissions inventory, diffusion model and receptor model. Among these categories, receptor models have been widely used because the methods are not limited by pollution discharge conditions, weather or terrain factors. The receptor models based on chemical analysis can be divided into two categories: one in which source profiles are needed, such as the Chemical Mass Balance (CMB) method; and one in which source profiles are not needed, such as the Positive Matrix Factorization (PMF) method. Because it is difficult to build large and accurate source profiles, we use the PMF method to perform source apportionment in our study. Previously, source apportionment studies in Beijing have mainly focused on single size fractions (i.e.,

PM$_{2.5}$, PM$_{10}$). Overall, the results showed that the contributions of major sources to PM$_{2.5}$ mass in Beijing exhibited seasonal and annual variations. The major sources of PM$_{2.5}$ mass in Beijing during 2000 were dust (20%), secondary sulfate (17%), secondary nitrate (10%), coal combustion (7%), diesel and gasoline exhaust (7%), secondary ammonium (6%), biomass aerosol (6%), cigarette smoke (1%), and vegetative detritus (1%) (Zheng et al., 2005). However, the PMF model identified six main sources of PM$_{2.5}$ in 2009-2010: soil dust, coal combustion, biomass burning, traffic and waste incineration emissions, industrial pollution, and secondary inorganic aerosols, with annual mean contributions of 16, 14, 13, 3, 28, and 26%, respectively, (Zhang et al., 2013b). In addition, the PMF method resolved 87 and 80% of the PM$_{2.5}$ in January and August 2004, respectively. The major sources were coal combustion (38% in January and 11% August), secondary sulfate (9% and 24%), secondary nitrate (10% and 8%), biomass burning (15% and 1%), motor vehicle emissions (8% and 15%) and road dust (7% and 8%) (Song et al., 2007). Previous studies regarding the size distributions of PM in urban Beijing have primarily focused on limited chemical species (Sun et al., 2013; Li et al., 2013; Yao et al., 2003) or have been conducted over short periods (Li et al., 2012a; Sun et al., 2010; Gao et al., 2012; Zhang et al., 2014b). To the best of our knowledge, no studies have been conducted on the source apportionment of size-resolved atmospheric particles based on long-term observations in urban Beijing.

To fill this knowledge gap, we observed size-resolved PM in urban Beijing from March 1, 2013 to February 28, 2014. In this study, we report the mass closure of particles based on a size-resolved chemical dataset obtained from haze and non-haze days over four seasons. The PMF method was combined with back trajectory cluster analysis to estimate the relative contributions of sources in different size fractions between haze and non-haze days and among different regional sources. These results will help policy-makers design emission control strategies and can serve as a database for future field measurements and modeling studies.

2. Materials and Methods

2.1. Sampling site

The experiment was performed from March 1, 2013, to February 28, 2014, at the Institute of Atmospheric Physics, Chinese Academy of Sciences (39°58′N, 116°22′E) (Fig. S1). The samplers were placed on the roof of a building approximately 15 m above the ground. The sampling site was located in Northwest Beijing between the 3rd and 4th ring roads. The site was selected to broadly represent the air pollution levels in urban Beijing because it was far from specific point emission sources.

2.2. Sampling collection

Two 9-stage samplers (Andersen Series 20-800, USA) with cutoff points of 0.43, 0.65, 1.1, 2.1, 3.3, 4.7, 5.8, and 9.0 μm, were used to simultaneously collect particles for 48 h (from 10:00 (local time, LT) on Monday to 10:00 LT on Wednesday) every week at a flow rate of 28.3 L min^{-1}. Overall, 52 sets of size-resolved PM samples were collected on quartz fiber filters and cellulose membranes (81 mm in diameter) during the study period. The quartz fiber filters were pre-fired (2 h at 800 ℃) to remove all organic material and were weighed before and after sampling using a microbalance with a sensitivity of ±0.01 mg. During the weighing processes, the filters eliminated static. Filters were conditioned in a dryer at 25±3 ℃ under a relative humidity (RH) of 22±3% for 72 h before each weighing. After re-weighing, the exposed filters were stored in a freezer at −20 ℃ to limit losses of volatile components loaded on the filters. To prevent the sampler from becoming blocked by particles during sampling, the samplers were cleaned using an ultrasonic bath for 30 min before each sampling. In addition, the sampling flow rates were calibrated before each sample was collected and were monitored using a flow meter during each sampling. Field blanks (a blank quartz filter and a blank cellulose membrane in each sampling) were used to determine any possible background contamination. All of the tools used during sampling and analysis were cleaned, and the operator wore plastic gloves. Meanwhile, the meteorological parameters used in this study, including visibility, temperature, RH,

171   wind speed (WS) and wind direction (WD), were collected at Beijing Capital

172   International Airport (http://english.wunderground.com) (Fig. S2).

173   **2.3 Chemistry analyses**

174   A quarter of each quartz filter was subjected to extraction in 25 ml of deionized

175   water (Millipore, 18.2 MΩ) in an ultrasonic bath for 30 min. The extraction liquid was

176   filtered and subsequently measured using ion chromatography (DIONEX, ICS-90,

177   USA) to determine the sodium (Na^+), NH_4^+, potassium (K^+), magnesium (Mg^{2+}),

178   calcium (Ca^{2+}), chloride (Cl^-), NO_3^- and SO_4^{2-} ion concentrations. For ion analysis,

179   the IC was equipped with a separation column (Ionpac CS12A 4×250 mm for cations

180   and Ionpac AS14A 4×250 mm for anions) and a suppressor (CSRS300–4 mm for

181   cations and ASRS 300–4 mm for anions). The eluents used for cations and anions

182   were 22 mmol L^{-1} MSA and 3.5 mmol L^{-1} Na_2CO_3/1 mmol L^{-1} $NaHCO_3$, respectively.

183   The ions were quantified by external standard curves every week, and one trace

184   calibration standard solution was used to check the curve each day. The limit of

185   detection was less than 0.02 μg m^{-3} for all ions when the injection volume was 100

186   μL.

187   Using another quarter of each quartz filter, the concentrations of OC and

188   elemental carbon (EC) were determined using a thermal/optical carbon aerosol

189   analyzer (DRI Model 2001A, Desert Research Institute, USA). Briefly, a punch

190   aliquot (0.495 cm^2) of a quartz fiber filter sample was heated stepwise in an oven at

191   140℃ (OC1), 280℃ (OC2), 480℃ (OC3) and 580℃ (OC4) under a pure helium

192   atmosphere to volatilize the OC before heating to 580℃ (EC1), 740℃ (EC2) and

193   840℃ (EC3) in a 2% oxygen-contained helium atmosphere for EC oxidation. At each

194   stage, the formed CO_2 was catalytically converted to CH_4 by a MnO_2 catalyst, and the

195   resulting CH_4 was measured using a flame ionization detector (FID). The analyzer

196   was calibrated before and after sample analysis by using a standard mixture of

197   CH_4 and CO_2. One sample was randomly selected from every 10 samples to conduct

198   duplicate sample analyses. The measurement errors were less than 10% for TC

199 (OC+EC), and the OC and EC concentrations in the field blanks were less than 1% of

200 the sample levels and were subtracted from the samples.

201 A quarter of the cellulose membrane was digested in a mixture of concentrated

202 HNO_3 (6 ml), HCl (2 ml) and HF (0.2 ml) in a closed vessel microwave digestion

203 system (MARS5, CEM Corporation, Matthews, NC, USA). Then, an Agilent 7500a

204 inductively coupled plasma mass spectrometer (ICP-MS, Agilent Technologies,

205 Tokyo, Japan) was used to determine the concentrations of 21 trace elements (TEs)

206 (sodium (Na), magnesium (Mg), Aluminum (Al), potassium (K), Calcium (Ca),

207 Manganese (Mn), Iron (Fe), cobalt (Co), Nickel (Ni), Copper (Cu), Zinc (Zn),

208 molybdenum (Mo), cadmium (Cd), Barium (Ba), thallium (Tl), Lead (Pb), thorium

209 (Th) and uranium(U)). A blank filter was analyzed in each batch for quality control.

210 Quantitative analysis was conducted using external calibration standards with

211 concentrations that were similar to those in the samples. In addition, internal standard

212 elements (^{45}Sc, ^{72}Ge, ^{115}In and ^{209}Bi) were added online during the metallic element

213 analysis.

214 The analysis methods, information regarding the instruments used in this study

215 (e.g., precision, calibration and detection limit) and quality control methods are

216 described elsewhere (Li et al., 2012b; Pan and Wang, 2015).

217 **2.4 Chemical mass closure**

218 Mass closure was used to discuss the relative contributions of the major

219 components in the PM. The chemical species were divided into the following seven

220 categories: sulfate-nitrate-ammonium (SNA), organic matter (OM), crustal materials

221 (CM), heavy metals (HM), EC, sea salt (SS) and liquid water (LW). The difference

222 between the mass weighted by microbalance and that reconstructed using the above

223 seven components was defined as unidentified matter (UM). The calculation methods

224 of the main components were described in our previous studies (Tian et al., 2014) and

225 are shown in Table S1 for convenience.

2.5 PMF model

PMF is an effective source apportionment receptor model (Karanasiou et al., 2009; Bullock et al., 2008; Paatero and Tapper, 1994; Paatero, 1997). In this study, EPA-PMF 3.0 was applied separately for the fine (the input data included the mass concentrations and chemical species in the particles with sizes of < 0.43, 0.43-0.65, 0.65-1.1 and 1.1-2.1 μm) and coarse (the input data included the mass concentrations and chemical species for particles with sizes of 2.1-3.3, 3.3-4.7, 4.7-5.8, 5.8-9 and > 9 μm) fractions. The numbers of samples analyzed for the fine and coarse fractions were 208 and 260, respectively. The chemical species included Na, Mg, Al, K, Ca, Mn, Fe, Co, Ni, Cu, Zn, Mo, Cd, Ba, Tl, Pb, Th, U, Na^+, NH_4^+, K^+, Mg^{2+}, Ca^{2+}, Cl^-, SO_4^{2-}, NO_3^-, OC and EC. The uncertainty of the concentration data, which was also the input data, was calculated as shown below.

If the concentration is less than or equal to the provided method detection limit (MDL), the uncertainty is calculated using the following equation:

$$Uncertainty = 5/6 \times MDL \qquad (1)$$

If the concentration is greater than the provided MDL, the calculation is

$$Uncertainty = \sqrt{(Error\ Fraction \times concentration)^2 + (MDL)^2} \quad (2)$$

In this study, the error fraction was estimated as 10 (the percent uncertainty multiplied by 100) for all of the chemical species, and the MDLs were similar to those reported in previous studies (Li et al., 2012a; Yang et al., 2009).

The base model was run 20 times with a different number of factors to obtain the best possible solution. During the first run, several species had a large number of absolute scaled residuals greater than 3, which indicated poor observed-predicted correlations. Then, these species were designated as "weak" and the model was rerun. When a reasonable solution was found, the bootstrapping technique was used to obtain the most meaningful results. Overall, 100 bootstrap runs were performed with a minimum r^2-value of 0.6. Of the 100 runs, the 6 factors were mainly mapped to a base factor in every run, which indicated a stable result.

254 Several criteria are important for ensuring a good PMF solution. First, the
255 modeled Q's should be within 50% of the theoretical value. Second, the optimum
256 number of factors should be determined by the criterion that each factor has a
257 distinctively dominant grouping of compounds. Third, the model uncertainty
258 produced by bootstrapping should be small. The principles are detailed elsewhere (Liu
259 et al.; Titos et al., 2014; Moon et al., 2008).

260 **2.6 Air mass back trajectory cluster**

261 The three-day backward trajectories arriving at the sampling site were calculated
262 using the National Oceanic and Atmospheric Administration (NOAA) HYSPLIT 4
263 model with a $0.5°\times0.5°$ latitude-longitude grid. The arrival level was set at 500 m
264 above ground level (a.g.l.). The HYSPLIT model was run four times each day at
265 starting times of 02:00, 08:00, 14:00, and 20:00 UTC during the sampling period.
266 Then, all of the trajectories were divided into different groups based on the horizontal
267 moving speed and direction of the air masses to form the trajectory clusters (Sirois
268 and Bottenheim, 1995; Wang et al., 2006b).

269 **3. Results**

270 **3.1 PM mass concentrations and chemical composition**

271 Table 1 describes the concentrations of the size-resolved mass and chemical
272 compositions during different seasons. The annual average concentrations of $PM_{2.1}$
273 (particulate matter with aerodynamic diameters less than 2.1 μm) and PM_9 (particulate
274 matter with aerodynamic diameters less than 9 μm) were 67.3 and 129.6 μg m^{-3},
275 respectively. Although the present level of $PM_{2.1}$ is significantly lower than that in
276 2009-2010 (135 μg m^{-3}) (Zhang et al., 2013b), it was more than times higher than the
277 National Ambient Air Quality Standard (NAAQS), which specifies an annual average
278 $PM_{2.5}$ of 15 μg m^{-3} (GB3095-2012, Grade I). In addition, PM_9 was approximately
279 three times the NAAQS annual average PM_{10} of 40 μg m^{-3} (Grade I). Thus, fine and
280 coarse particles, defined in this study as particles with sizes < 2.1 ($PM_{2.1}$) and 2.1-9.0
281 μm ($PM_{2.1-9}$), respectively, are important for PM in urban Beijing.

282   As shown in Table 1, the primary components of $PM_{2.1}$ are OC (24.5% of $PM_{2.1}$),

283   SO_4^{2-} (14.7%), NO_3^- (11.2%) and NH_4^+ (9.2%). In contrast, Ca (3.5±1.5 µg m^{-3}), EC

284   (2.0±1.8 µg m^{-3}) and other species accounted for approximately 40% of $PM_{2.1}$. The

285   composition of the coarse particles was different from the composition the fine

286   particles ($PM_{2.1}$). In this study the highest contribution to $PM_{2.1-9}$ was Ca (16.3% of

287       $PM_{2.1-9}$), followed by OC (15.5%), NO_3^- (4.5%), Fe (4.1%) and SO_4^{2-} (3.5%). These

288   species accounted for approximately 44% of $PM_{2.1-9}$. The mass closure of

289   size-resolved particles is discussed in detail below (Sect. 4.2).

290   **3.2 Seasonality**

291   The concentrations of $PM_{2.1}$ were greatest during winter (December to February,

292   76.8 µg m^{-3}), followed by spring (March to May), summer (June to August) and

293   autumn (September to November), with concentrations of approximately 65 µg m^{-3}

294   during the latter three seasons (Table 1). In contrast, the concentrations of $PM_{2.1-9}$

295   decreased in the following order spring > autumn > winter > summer.

296   The seasonal dependency varied with species. For most of the species that were

297   enriched in the fine mode (with a $PM_{2.1}/PM_9$ chemical concentration ratio greater than

298   0.5, including NH_4^+, Tl, Cd, Pb, SO_4^{2-}, NO_3^-, EC, K^+, Zn, Cl^-, OC, Cu, Na, Na^+, Mo

299   and K), in the compositions of $PM_{2.1}$ and $PM_{2.1-9}$ exhibited similar seasonal variations,

300   with the $PM_{2.1}$ mass concentration being higher during colder seasons. However, the

301   seasonal dependence of the concentration of certain species in $PM_{2.1}$ differs from the

302   typical seasonal variation. For example, the concentrations of SO_4^{2-} and NH_4^+ in

303   spring and summer were higher than those in autumn and winter. This result was

304   consistent with the seasonal variability of SO_4^{2-} and NH_4^+ in $PM_{2.5}$ in 2009-2010

305   (Zhang et al., 2013b).

306   In addition, the OC concentrations in $PM_{2.1}$ decreased as follows: summer (20.2

307   µg m^{-3}) > spring (16.5 µg m^{-3}) > winter (16.2 µg m^{-3}) > autumn (13.4 µg m^{-3}). The

308   high OC concentrations during the summer primarily resulted from the photochemical

309   generation of more secondary organic carbon (SOC). This result can be confirmed by

310　the OC/EC ratios, which exhibited the following seasonal pattern: summer (16.7) >

311　spring (12.7) > autumn (6.7) > winter (4.9). Because EC primarily arises from

312　primary combustion emissions, the OC/EC ratios were used to evaluate the

313　contributions from secondary organic carbon (Cao et al., 2007).

314　　For species enriched in the coarse mode ($PM_{2.1-9}$) (with a $PM_{2.1}/PM_9$ chemical

315　concentration ratio below 0.5, including Ni, Mn, U, Co, Mg^{2+}, Th, Al, Ba, Mg, Ca and

316　Ca^{2+}), their $PM_{2.1}$ and $PM_{2.1-9}$ concentrations demonstrated typical seasonal variations,

317　with higher concentrations observed during the spring and autumn (or winter) due to

318　the influences of re-suspended soil dust. Re-suspended soil dust may result from both

319　long transport dust and local anthropogenic sources (construction dust and mechanical

320　abrasion processes). The relatively high wind speed during spring facilitated the

321　ascent of road dust into the atmosphere and resulted in the relatively high value of the

322　species in the coarse mode (Liu et al., 2014a).

323　**3.3 Size distribution**

324　　The size distributions of the mass concentrations and the chemical species are

325　shown in Fig. 1 and Fig. S3. In each season, the size distribution of the mass

326　concentrations was bimodal. The fine modes commonly showed maxima at 0.65-1.1

327　μm in spring, autumn and winter and 0.43-0.65 μm in summer. The coarse modes

328　showed maxima at 4.7-5.8 μm in all of the seasons. As shown in Fig. 1, the peak of

329　the fine mode was broader in winter than in the other seasons, indicating the

330　complexity of the emissions in winter (Sun et al., 2013). Emissions from coal

331　combustion for heating are greater during winter, especially for retail coal combustion

332　in surrounding areas, which is difficult to control (Wang et al., 2006a). However, the

333　meteorological conditions in winter are unfavorable for the diffusion of fine particles

334　and precursors (SO_2, NOx, VOCs), making secondary particle emissions more

335　complex.

336　　The chemical species can generally be divided into three groups based on their

337　size distributions. First, SO_4^{2-}, NO_3^-, NH_4^+, EC, Zn, Cd, Pb and Tl were abundant in

338   the fine mode, which exhibited maxima at 0.43-0.65 μm or 0.65-1.1 μm in all four

339   seasons that corresponded to coal and motor vehicle sources (Li et al., 2013). Second,

340   Ca^{2+}, Mg^{2+}, Ba, Mg, Al, Ca, Fe, Co, Ni, Th and U were primarily concentrated in the

341   coarse mode from 4.7 to 5.8 μm, which suggested natural sources from soil dust or

342   mechanical abrasion processes (Sun et al., 2013; Maenhaut et al., 2002a). Third, OC,

343   Cl^-, K^+, Na^+, Na, K, Mn, Cu and Mo exhibited typical bimodal distributions, and the

344   amplitude of the fine mode was well correlated with that of the coarse mode. These

345   species exhibited maxima at 0.43-0.65 μm or 0.65-1.1 μm and peaked at 4.7-5.8 μm in

346   the coarse mode. Cl^- and K^+ are good biomass burning tracers (Du et al., 2011), and

347   Mn and Cu are good industrial pollution tracers. Hence, the species in the third group

348   may represent mixed sources from biomass burning and industrial pollution.

349   The size distribution of the mass concentration and OC peaked at 0.43-0.65 μm in

350   summer and 0.65-1.1 μm in winter. Because the primary organic carbon emissions

351   were relatively stable across the four seasons, the size distribution differences in the

352   fine mode primarily resulted from the generation of SOC (Duan et al., 2005). The

353   difference between summer and winter indicated that the SOC formation in summer

354   was enhanced due to photochemical reactions and primarily accumulated in

355   "condensation mode" (Zhang et al., 2008). However, because photochemistry is

356   typically weak in winter, the SOC generation mainly resulted from the high RH and

357   high precursor concentrations, including volatile organic compounds (VOCs) from

358   biological (such as monoterpene and sesquiterpene) and anthropogenic sources (such

359   as aromatics) (Jacobson et al., 2000). Thus, VOCs primarily accumulated in "droplet

360   mode" (Cao et al., 2007). Previously, our findings indicated that weakening incident

361   solar radiation reduces the formation of SOC formation in the smaller size fraction

362   and that high RH plays an important role in the generation of SOC in larger size

363   fractions (Tian et al., 2014).

364   **3.4 Ion balance**

365   We calculated the ion balance for each size fraction, which was used to evaluate

366 the ion deficiency between cations and anions in the PM (Fig. S4). The average

367 equivalent ratio of total cations (Na^+, NH_4^+, K^+, Mg^{2+}, and Ca^{2+}) to total anions (SO_4^{2-},

368 NO_3^- and Cl^-) ranged from 0.95 to 2.50, with lowest ratio occurring in the 1.1-2.1 μm

369 size fraction and highest ratio occurring in the 4.7-5.8 μm size fraction. The total

370 cation to total anion ratio in the fine particles was near unity throughout the year,

371 which indicated excellent charge balance and high data quality. The slope for the fine

372 mode particles was mainly greater than 1 because the concentrations of CO_3^{2-} and

373 HCO_3^- were not determined.

374   Fig. S5 shows good correlations between the NH_4^+ and SO_4^{2-} concentrations in

375 the fine particles for the data sets in different seasons, with NH_4^+/SO_4^{2-} equivalent

376 ratios greater than 1 (spring (1.92) summer (1.79), autumn (1.01), winter (1.36)),

377 revealing the dominance of $(NH_4)_2SO_4$. Next, we calculated the molar ratio of NH_4^+ to

378 $[NO_3^- + SO_4^{2-}]$, which was slightly higher than unity in spring (1.25) and summer

379 (1.33) and indicated the presence of NH_4NO_3 in the fine aerosols. However, the ratios

380 were less than one in the autumn (0.78) and winter (0.68), which indicated that NO_3^-

381 could be present in chemical forms other than NH_4NO_3.

382   For the coarse mode particles, the NH_4^+/SO_4^{2-} equivalent ratios in spring (0.78)

383 summer (0.68) and autumn (0.58) were less than 1 but greater than 0.5, which

384 indicated the dominance of $(NH_4)_2SO_4$ and NH_4HSO_4. By contrast, the ratio in winter

385 (1.33) was greater than unity, and the equivalent ratio of NH_4^+ to $[NO_3^- + SO_4^{2-}]$ in

386 winter was less than unity.

387 **4. Discussion**

388 **4.1 Size-resolved aerosol compositions on non-haze and haze days**

389   Fig. 2 illustrates the size-segregated PM mass concentrations during the sampling

390 period. Haze is defined as a weather phenomenon in which a high concentration of

391 fine particles occur that result in a visibility of less than 10 km at a relative humidity

392 (RH) of less than 90% (Sun et al., 2006; Tan et al., 2009; Zhuang et al., 2014). Thus,

393 we used visibility and RH to determine the haze/no-haze days as follows: sampling

394　days with visibility < 10 km and RH < 90% were defined as haze days and sampling

395　days with visibility > 10 km and RH < 90% were defined as non-haze days. During

396　the observation period, 12 sets of size-resolved PM samples were collected during

397　non-haze days and 19 sets were collected during haze days (marked in Fig. 2). Of the

398　remaining 21 sets, 15 sets were collected during rain, snow or fog days and 6 sets

399　were collected during dust days (visibility < 10 km, RH < 40%). These samples were

400　excluded from the dataset when we discussed the differences between haze and

401　non-haze days.

402　**4.1.1 Concentration enhancement ratios**

403　Table S2 describes the annual average concentrations of the size-resolved mass

404　and chemical compositions on haze and non-haze days over four seasons. The annual

405　average $PM_{2.1}$ and $PM_{2.1-9}$ concentrations on haze days were 86.1 and 72.6 μg m^{-3},

406　which were 2.6 and 1.4 times those on non-haze days, respectively. Therefore, it is

407　evident that fine particles significantly accumulated during the haze pollution period

408　(Wang et al., 2014). In addition, the mass concentration enhancement ratio from

409　non-haze to haze days ($R_{H/N}$) was examined during all four seasons.

410　$$R_{H/N} = C_H/C_N, \qquad\qquad (3)$$

411　C_H—Concentration of chemical species on haze days;

412　C_N—Concentration of chemical species on non-haze days.

413　The $R_{H/N}$ for fine particles revealed a typical seasonality, with the highest value

414　occurring in winter (5.6) and the lowest value occurring in the spring (1.8). The $R_{H/N}$

415　for coarse particles was lower than that for fine particles, which ranged from 1.1 to

416　1.9 and decreased as follows: summer > autumn > winter > spring. The higher $R_{H/N}$

417　values for fine particles further indicated the importance of fine particles in haze

418　pollution.

419　We calculated the $R_{H/N}$ ratios for chemical species in each size fraction. Based on

420　the $R_{H/N}$ ratios variations with increasing size fraction, all the species can be divided

421　into three groups. First, OC, NO_3^-, SO_4^{2-}, NH_4^+, K^+, Cl^-, K, Mn, Ni, Cu, Zn, Pb and

422   Tl exhibited high $R_{H/N}$ ratios in fine mode and a peak value in size fraction 0.65-1.1

423   μm or 1.1-2.1 μm. Second, $R_{H/N}$ ratios of Na^+, Mg^{2+}, Ca^{2+}, Mg and Fe increased with

424   increasing size fraction. Third, EC, Na, Al, Ca, Co. Mo, Cd, Ba, Th and U, $R_{H/N}$ ratios

425   of these species first increased and then decreased with increasing size fraction and

426   exhibited highest $R_{H/N}$ ratios in size fraction 1.1-2.1μm, 2.1-3.3 μm or 3.3-4.7μm.

427   The annual average $R_{H/N}$ of the chemical components in $PM_{2.1}$ ranged from 0.8 to

428   5.5, with values greater than 2.6 for NO_3^-, SO_4^{2-}, NH_4^+, Pb, Tl and Cd. This finding

429   was consistent with the findings of previous studies (Tian et al., 2014; Sun et al.,

430   2013), indicating that coal and motor vehicle sources played important roles in haze

431   pollution (Li et al., 2013). Regarding the seasonal variations, the particulate mass and

432   most of the species exhibited the highest $R_{H/N}$ in winter, which indirectly showed that

433   severe haze events primarily occurred in winter.

434   Simultaneously, the annual average $R_{H/N}$ of the chemical components in $PM_{2.1-9}$

435   ranged from 0.8 to 5.3, which was similar to that for fine particles. The NH_4^+, NO_3^-,

436   SO_4^{2-}, Cd, EC, Cl^-, Pb, Tl, Na^+, OC, Zn and K^+ in the coarse fraction exhibited $R_{H/N}$

437   values greater than 1.4. Among these species, Pb, Cd and Tl had high toxicity. Thus,

438   the mitigation of particles with diameters greater than 2.1 μm cannot be neglected

439   during haze events. Similar to $PM_{2.1}$, most of the species in the coarse fraction

440   exhibited the highest $R_{H/N}$ in winter. In contrast, the highest $R_{H/N}$ values for Na^+, K^+

441   and Cl^- in the coarse fraction were observed in summer, which was similar to the

442   results of the mass concentration. The highest $R_{H/N}$ for Na^+, K^+ and Cl^- in the coarse

443   fraction was observed in summer, mainly due to low concentrations on non-haze days

444   and relatively high concentration of haze days. The lower concentrations of coarse

445   particles in summer were likely related to greater precipitation during this season.

446   High concentrations of K^+ and Cl^- in coarse mode on haze days were mainly

447   associated with biomass burning (Du et al., 2011). One of the samples that

448   represented a haze day in summer was collected between June 17 and 19. During this

449 period, burning wheat straw in the surrounding areas affected both fine and coarse

450 particle pollution in Beijing (Wang et al., 2015; Yan et al., 2015; Cheng et al., 2014).

451   The concentrations of NO_3^-, SO_4^{2-} and NH_4^+ in the fine and coarse particles were

452 higher on haze days than on non-haze days. These species are involved in

453 heterogeneous chemical reactions (Sun et al., 2013). Figs. S6a and b show good

454 correlations between NH_4^+ and SO_4^{2-} in fine particles from non-haze and haze days,

455 with an equivalent NH_4^+/SO_4^{2-} ratio greater than unity (ranging from 1.5-1.6). This

456 result reveals the dominance of $(NH_4)_2SO_4$. Next, we calculated the equivalent ratio of

457 NH_4^+ to $[NO_3^- + SO_4^{2-}]$ (Figs. S6c and d), which was slightly higher than unity on

458 non-haze days and indicated the presence of NH_4NO_3 in the fine mode aerosols.

459 However, on haze days, the ratios were less than unity, which indicated that NO_3^-

460 may be present in chemical forms other than NH_4NO_3.

461 **4.1.2 Peak shifts**

462   Fig. 3 compares the annual average mass concentration size distributions on

463 non-haze and haze days, which were considered bimodal, with the peaks

464 corresponding to the fine modes located at 0.65-1.1 μm and those corresponding to

465 the coarse modes peaking at 4.7-5.8 μm. No significant differences in the average size

466 distributions were found between haze and non-haze days in each season (Fig. 3).

467 This result was inconsistent with the results obtained from early 2013, which showed

468 that the peak mass concentration of fine mode particles shifted from 0.43-0.65 μm on

469 clear days to 0.65-1.1 μm on lightly polluted days and 1.1-2.1 μm on heavily polluted

470 days (Tian et al., 2014).

471   However, in this study, peak shifts from 0.43-0.65 μm on non-haze days to

472 0.65-1.1 μm on haze days were observed when considering the annual average size

473 distributions of SO_4^{2-}, OC, NO_3^-, NH_4^+, Cl^-, K^+ and Cd. The peak values of these

474 species at 0.43-0.65 μm in the fine mode on non-haze days correspond to the

475 "condensation mode" due to the transformation of precursors and heterogeneous

476 reactions, while those at 0.65-1.1 μm on haze days correspond to the "droplet mode",

477 which likely form in clouds or through aqueous-phase chemical reactions (Sun et al.,

478 2013). The high RH during haze days may facilitate the formation of "droplet mode"

479 particles, and a similar finding was previously reported (Sun et al., 2013; Zhang et al.,

480 2013a). However, this result was slightly different from that observed in early 2013,

481 which showed that the peak concentration of NH_4^+, SO_4^{2-} and NO_3^- in fine mode at

482 1.1-2.1 μm on heavily polluted days resulted from the high RH and high precursor

483 concentrations (Tian et al., 2014).

484 We also compared size distributions of chemical species between haze and

485 non-haze days in different seasons. The results showed that the peak concentration of

486 OC, SO_4^{2-}, Cl^- and Mn in fine mode particles shifted from 0.43-0.65 μm on non-haze

487 days to 0.65-1.1 μm on haze days in spring. However, species exhibited peak shifts in

488 summer were EC, K^+, NO_3^- and Ni. Besides, in autumn, fine mode peak concentration

489 of EC, NH_4^+, SO_4^{2-}, NO_3^-, Cd and Cu shifted from 0.43-0.65 μm on non-haze days to

490 0.65-1.1 μm on haze days. Meanwhile, NH_4^+, SO_4^{2-}, NO_3^-, K^+, Cl^-, Cd, Zn and Pb

491 exhibited fine mode peak shifts from non-haze days to haze days in winter. These

492 indicated that there are different formation mechanisms for haze in different seasons.

493 **4.2 Mass closure studies**

494 **4.2.1 Non-haze vs. haze days**

495 Mass closure studies showed that SNA, OM and CM dominated the fine particles,

496 which accounted for 87.7% and 76.6% of the $PM_{2.1}$ mass on non-haze and haze days,

497 respectively (Figs. 4a-d). Generally, the contribution of OM to $PM_{2.1}$ was greater than

498 the contributions of SNA and CM. However, during haze episodes in cold seasons,

499 SNA was more significant than OM because the high RH and precursor emissions

500 (i.e., SO_2) promoted the generation of SNA (Tian et al., 2014). The contributions of

501 SNA to the fine particle mass were significantly higher on haze days than on non-haze

502 days. In contrast, the CM and OM contributions decreased from non-haze to haze

503 days.

504   High total CM, OM and SNA contributions were also observed in $PM_{2.1-9}$, which

505   accounted for 58.5% and 54.3% of the total $PM_{2.1-9}$ mass on non-haze days and haze

506   days, respectively. The contributions of these species in coarse particles decreased as

507   follows on haze and non-haze days: CM > OM > SNA. However, in fine particles, the

508   order was OM > CM > SNA on non-haze days and OM > SNA > CM on haze days.

509   In summary, the relative contributions of OM and CM to the particle mass decreased

510   from non-haze to haze days, and the relative contribution of SNA increased from

511   non-haze days to haze days.

512   **4.2.2 Differences among size fractions**

513   For different size fractions, the contributions of OM, HM and EC were greatest in

514   the < 0.43 μm fraction (41.3%, 2.2% and 7.0%, respectively). The contribution of

515   SNA, which is primarily formed from precursors via heterogeneous reactions, was

516   greatest in the 0.43-0.65 μm fraction (34.5%), which is within the "condensation

517   mode" (Fig. 4e). The contribution decreased as the size increased, which indicated

518   that these anthropogenic species primarily accumulated in the fine mode. However,

519   the minimal contributions of OM, HM, EC and SNA occurred in the 5.8-9 μm

520   (6.9%), > 9 μm (0.7%), 4.7-5.8 μm (0.9%) and > 9 μm (4.1%) size fractions,

521   respectively. In addition, CM and SS exhibited similar size fraction variations, which

522   increased from < 0.43 μm to 3.3-4.7 μm and then decreased. The highest contributions

523   of CM and SS appeared in the 3.3-4.7 μm fraction and were 35.6% and 4.9%,

524   respectively.

525   **4.2.3 Unidentified mass**

526   The reconstructed PM mass concentrations were compared with the gravimetric

527   values, as shown in Fig. S7. The results were correlated with one another in the

528   different size fractions, with R^2 values for $PM_{1.1}$ (particulate matter with aerodynamic

529   diameter lower than 2.5 μm), $PM_{2.1}$, PM_9 and TSP (total suspended particulate matter)

530   of 0.69, 0.79, 0.70 and 0.60, respectively. In addition, the contributions of the

531   unidentified components ranged from 0.4% to 57.8% and increased as the sizes

532 increased. The large unidentified components in the coarse particles potentially

533 resulted from underestimating CM (Hueglin et al., 2005; Sun et al., 2004). In this

534 study, Si was estimated as 3.42 times Al, and the ratios were applied to all of the size

535 fractions. This assumption may be underestimated because the Si/Al ratio could

536 increase with size. For example, the contribution of CM to coarse particles reached

537 42.4% based on the Si/Al ratio of 6.0 in $PM_{2.5-10}$, which was previously reported in

538 Beijing (Zhang et al., 2010). Thus, the contribution of the unidentified components

539 decreased from 38.5% to 25.5% for the total $PM_{2.1-9}$ mass.

540 **4.3 Source apportionment**

541 **4.3.1 Fine and coarse particles**

542   Six $PM_{2.1}$ and seven $PM_{2.1-9}$ sources were identified by PMF analysis, respectively.

543 Fig. 5(a) and (b) show the profiles of each source in the fine and coarse fractions,

544 respectively, and the percentages of species apportioned by each source. The sources

545 identified in the fine fraction were named as secondary inorganic aerosol (SIA), coal

546 combustion, biomass burning, industrial pollution, road dust and vehicle emissions.

547 Coarse fraction sources were SIA, coal combustion, biomass burning, industrial

548 pollution, road dust, mineral dust and organic aerosol. Together these sources

549 represented 91.6% and 86.6% of $PM_{2.1}$ and $PM_{2.1-9}$, respectively.

550   **Secondary inorganic aerosol (SIA)**

551   The first source was relevant to secondary inorganic aerosol (SIA), which was

552 identified in both fractions and was typically characterized by significant amounts of

553 SO_4^{2-}, NO_3^- and NH_4^+. SIA contributed 25.1% (16.9 μg m^{-3}) and 9.8% (6.1 μg m^{-3}) to

554 the fine and coarse particles, respectively. Contributions of SIA to both $PM_{2.1}$ and

555 $PM_{2.1-9}$ followed the order winter (29.5% to $PM_{2.1}$ and to 16.5 to $PM_{2.1-9}$) > spring

556 (27.2% and 9.3%) > autumn (20.3% and 7.8%) > summer (18.1% and 5.7%). The SIA

557 contribution to the fine particles was similar to that in Beijing for 2009-2010 (Zhang

558 et al., 2013b).

559   **Coal combustion**

560   The second source, coal combustion, was also identified in both fractions and was

561   characterized by elevated OC and EC, concentrations (Tian et al., 2010;Kang et al.,

562   2011). The contribution of this source to $PM_{2.1}$ was 17.7% (11.9 μg m^{-3}), which

563   closely approximates the value of 19% derived in Beijing for 2009-2010 (Zhang et al.,

564   2013b). In addition to its contribution to $PM_{2.1}$, coal combustion significantly

565   contributed to $PM_{2.1-9}$ (7.8%, 4.9 μg m^{-3}). The contributions of coal combustion to

566    $PM_{2.1}$ and $PM_{2.1-9}$ exhibited similar seasonal patterns of winter (27.0% to $PM_{2.1}$ and

567   9.4% to $PM_{2.1-9}$) > autumn (17.5% and 8.9%) > summer (14.5% and 6.6%) > spring

568   (9.6% and 6.4%).

569   **Biomass burning**

570   The third source, biomass burning, was also identified in both fractions and was

571   represented by high Cl^- and K^+ contents (also K, which is an excellent tracer of

572   aerosols from biomass burning) (Du et al., 2011) and is rich in Na^+ (Moon et al.,

573   2008). The contribution in $PM_{2.1}$ was 8.6%, which was significantly higher than the

574   6.9% contribution in $PM_{2.1-9}$. This finding is expected because biomass burning

575   contributed much more to the fine particles than the coarse particles (Cheng et al.,

576   2014). Its contributions to $PM_{2.1}$ and $PM_{2.1-9}$ demonstrated a typical seasonal variation,

577   with higher concentrations observed in spring (11.1% to $PM_{2.1}$ and 11.8% to $PM_{2.1-9}$)

578   and winter (13.5% and 10.2%).

579   **Industrial pollution**

580   The fourth source was industrial pollution, which was also identified in both

581   fractions and was characterized by high Fe, Ni, Co, Mg, Al and Ca, contents in fine

582   size fraction and by high Cd, Pb, Tl, Zn and Cu contents in coarse fraction (Karnae

583   and John, 2011). The contribution from this source was 12.1%, which is slightly

584   higher than the 5.1% contribution for coarse particles. Its contributions to $PM_{2.1}$ and

585    $PM_{2.1-9}$ demonstrated a typical seasonal variation, with higher concentrations observed

586   in summer (16.7%) and autumn (14.5%) for fine fraction and with higher

587   concentrations observed in winter (5.7%) and spring (7.9%).

Road dust

The fifth component, road dust, was also identified in both fractions and was related to the high loading of crustal elements, such as Al, Ca (Ca^{2+}), Mg (Mg^{2+}), Na (Na^+) and Co, Ni, Cu (Titos et al., 2014;Vecchi et al., 2008). This source represented 8.4% and 10.9% of the total mass in the fine and coarse fractions, respectively. Contributions of road dust to both $PM_{2.1}$ and $PM_{2.1-9}$ followed the order winter (9.9% to $PM_{2.1}$ and to 18.3% to $PM_{2.1-9}$) > autumn (10.2% and 16.0%) > spring (4.9% and 9.3%) > summer (6.3% and 4.7%).

Vehicle emissions

The sixth source, vehicle emissions, which was only identified in fine fraction and was characterized by high Pb, Cd, Zn, K and EC (Begum et al., 2004; Karnae and John, 2011). EC primarily arises from engines; Zn and K are found in tailpipe emissions; Pb is present in motor and fuel oil combustion (Yang et al., 2013). This source explained 19.6% of $PM_{2.1}$. Contributions of vehicle emissions $PM_{2.1}$ were higher in spring and summer. During 2000 and the period 2009-2010, the contributions from vehicles to the fine particles in Beijing were 7% and 4%, respectively (Zheng et al., 2005;Zhang et al., 2013b), and these values were lower than those reported in this study. The source in previous studies might be primary emissions from vehicles, however, in addition to primary emissions, vehicles also emit large amounts of NO_x precursors, which contributed significantly to the PM via the generation of secondary particles. This important contribution was included in the SIA source but not in the primary emissions factor. Thus, the contributions of traffic emissions to PM will be much higher than the present value if we further consider the secondary formation of NO_3^- from NO_x. Besides, vehicles equipped with three-way catalysts are an important source of NH_3, which may also contribute to the SIA.

Mineral dust

The seventh component, mineral dust, was only identified in coarse fraction and

616 was related to the high loading of crustal elements, such as Al, Fe, Ca (Ca^{2+}), Mg, K

617 (K^+) (Titos et al., 2014;Vecchi et al., 2008). This source might mainly indicate local

618 and long-range transported dust aerosols and represented 22.6% to the total mass in

619 coarse fraction. It exhibited a typical seasonal variation, with higher concentrations

620 observed in spring (36.2%).

621 **Organic aerosol**

622 The eighth source was relevant to organic aerosol, which was only identified in

623 coarse fraction and was typically characterized by significant amounts of OC. Organic

624 aerosol contributed 23.6% (14.7 μg m^{-3}) to the coarse particles. Its contributions to

625 $PM_{2.1-9}$ demonstrated a typical seasonal variation, with higher concentrations observed

626 in summer (51.3%).

627 **4.3.2 Non-haze vs. haze days**

628 Figs. 6a-d illustrate the contributions of the six sources to the fine and seven

629 source to the coarse particles on clear and haze days. On haze days, the contributions

630 of SIA, coal combustion, biomass burning, industrial pollution, road dust and vehicle

631 emissions, were 18.4%, 13.8%, 16.0%, 12.5%, 12.8% and 17.5% to the fine fractions

632 and the contributions of SIA, coal combustion, biomass burning, industrial pollution,

633 road dust, mineral dust and organic aerosol were 13.4%, 8.7%, 7.8%, 5.2%, 8.3%,

634 24.4% and 19.5% to the coarse fractions. The contributions of these factors on haze

635 days were higher than those on non-haze days, except road dust, and industrial

636 pollution to fine fraction and mineral dust to coarse fraction particles. Additionally,

637 the $R_{H/N}$ of the six sources was highest for SIA (6.9 to fine particles vs. 10.1 to coarse

638 particles), followed by vehicle emissions (4.3 to fine particles), biomass burning (2.8

639 vs. 2.2), coal combustion (1.9 vs. 2.5), mineral dust (1.7 to coarse particles), organic

640 aerosol (1.47 to coarse particles), industrial pollution (1.2 vs. 2.1) and, finally, road

641 dust (0.7 vs. 0.7). The high $R_{H/N}$ values indicated that enhanced secondary conversion

642 could occur in the atmosphere during heavy-pollution days. Furthermore, primary

643 particles and gaseous precursors from coal combustion and traffic emissions played

644   important roles in haze pollution.

645   The strong contribution of mineral dust and road dust on non-haze days was

646   primarily due to high wind speeds, which transported large quantities of particles from

647   nearby areas outside of the city. Similarly, the industrial pollution affecting urban

648   Beijing primarily arose from the surrounding areas, and the high wind speeds on

649   non-haze days transported large quantities of industrial emission particles into Beijing

650   from outside areas. However, on haze days, particles from coal combustion, primary

651   emissions from vehicles, biomass burning and secondary formation were important.

652   Thus, strict control over particles and gaseous precursor emissions from coal and oil

653   combustion is required.

654   **4.3.3 Difference among the size fractions**

655   Fig. 7 shows that the relative contributions of each identified source varied

656   substantially among size fractions. Among all the sources, SIA and mineral dust (road

657   dust for fine fractions and road dust plus mineral dust for coarse fractions), which

658   were also identified in the mass closure analyses, exhibited relative orders in the eight

659   size fractions that were similar to those in the mass closure results. However, the

660   contributions of SIA in the eight size fractions were different from the contributions

661   of SNA obtained by mass closure (i.e., 3.2-30.4% for SIA vs. 4.1-34.5% for SNA).

662   The contribution of mineral dust increased with particle size, with the highest

663   contribution found observed in the 3.3-4.7 μm fraction (37.4%) and the lowest

664   contribution observed in the 0.65-1.1 μm fraction (5.2%). These results were

665   consistent with the mass closure results, which indirectly verified the reliability of the

666   PMF results.

667   The contributions of the other sources (coal combustion, biomass burning,

668   industrial pollution) generally decreased with increasing size fraction and were

669   present at high concentrations in the fine and coarse modes. For example, the

670   contributions of coal combustion to the total mass in the different size fractions

671   ranged from 7.2% to 42.2%, with the highest proportion found in the <0.43 μm

672 fraction (42.2%) and a relatively high proportion found in the 3.3-4.7 μm fraction

673 (8.5%). Similarly, the contributions of industrial pollution ranged from 2.4% (5.8-9

674 μm) to 15.9% (<0.43 μm),.The concentrations of biomass burning were approximately

675 8% with high proportions in the fine (< 0.43 μm) and (1.1-2.1 μm). The complexity of

676 the source apportionment results for different size fractions indirectly verifies that the

677 source apportionment of $PM_{2.5}$ cannot provide comprehensive source information

678 because it neglects the importance of the sources that dominated the coarse size

679 fractions. For example, the highest proportion of industrial pollution was observed in

680 the 3.3-4.7 μm size fraction.

681   To further examine the importance of source apportionment in the different size

682 fractions, we compared the source apportionment results for the corresponding size

683 sub-fractions within $PM_{2.1}$ and $PM_{2.1-9}$. As shown in Fig. 7, the contributions of each

684 source to PM significantly varied among the size fractions within $PM_{2.1}$ and $PM_{2.1-9}$.

685 The contributions of SIA, coal combustion, vehicle emissions and road dust to the size

686 fractions within $PM_{2.1}$ ranged from 8.9% to 30.4%, from 10.1% to 42.2%, from 11.4%

687 to 27.7% and from 5.2% to 10.5%, respectively. In addition, significant differences

688 were observed among the size fractions within $PM_{2.1-9}$ regarding the contributions of

689 SIA, industrial pollution and organic aerosol, which ranged from 3.2% to 23.6%, from

690 2.4% to 8.5% and from 13.8% to 27.9%, respectively. This result further indicated the

691 importance of source apportionment for subdivided size fractions within $PM_{2.1}$ and

692 $PM_{2.1-9}$.

693 **4.3.4 Back trajectory cluster analysis**

694   Approximately 34% of $PM_{2.5}$ in urban Beijing can be attributed to sources outside

695 of Beijing, and the contribution increased 50-70% during sustained wind flow from

696 the south Hebei Province (Streets et al., 2007). This modeling result indicated the

697 importance of the regional transport effect on fine particles in urban Beijing, but the;

698 However the source apportionment based on size-resolved chemical measurements

699 was previously unavailable.

700   To fill this gap, the annual data were subjected to back trajectory cluster analysis

701   to identify the source regions and primary atmospheric circulation pathways that

702   influence the PM concentration and chemical species (Fig. 8). The air masses that

703   reach Beijing follow seven main paths, including four from the northwest (NW, C1,

704   C2, C5 and C7) and one from southwest (SW, C3), one from the southeast (SE, C4)

705   and one from the northeast (NE, C6). Fig. S8 shows the size distributions of the mass

706   concentrations within each trajectory cluster. The size distributions of the mass

707   concentrations reveal large differences between the different trajectory clusters in the

708   fine mode, especially in the peak size fraction (0.65-1.1 μm).

709   Because regional transport has stronger impacts on fine particles than on coarse

710   particles, with the largest differences observed between trajectory clusters, we only

711   report the identified $PM_{2.1}$ sources associated with different trajectory clusters to

712   determine the effects of the different source regions (Fig. 8). The polluted air mass

713   trajectories are defined as those with $PM_{2.1}$ concentrations higher than the annual

714   mean of 67.3 $\mu g\ m^{-3}$.

715   Although the greatest proportion of the trajectories (approximately 36%) was

716   assigned to the NW cluster, this cluster was associated with the lowest $PM_{2.1}$

717   concentration of 47.6 $\mu g\ m^{-3}$. Thus, this cluster has a weaker effect on PM pollution in

718   Beijing. The long and rapidly moving trajectories were disaggregated into this group,

719   and members of this cluster have extremely long transport patterns in which some

720   parts cross over Mongolia, Inner Mongolia and northwest Hebei. In addition, this

721   cluster was dominated by coal combustion (19%) and SIA (18%).

722   The SW cluster is the most important transport pathway with a large number of

723   trajectories (approximately 32%) and a high $PM_{2.1}$ concentration (79.9 $\mu g\ m^{-3}$). The

724   trajectories belonging to the SW cluster are characterized by the shortest trajectories,

725   which indicate the closest and slowest-moving air masses that are primarily

726   transported from Hebei and south Beijing. Most of the extreme episodes in this group

727   were probably enriched by regional and local emission sources. As shown in Fig. 8,

728   this cluster was dominated by SIA (27%) and coal combustion (19%).

729   As shown in Fig. 8, only 15% and 16% of the trajectories were assigned to the SE

730   and NE clusters, respectively. However, these trajectories were associated with high

731    $PM_{2.1}$ concentrations (87.0 and 67.4 μg m^{-3}). The SE cluster typically followed a flow

732   pattern over north Jiangsu and Shandong and was dominated by SIA (31%) and

733   vehicle emissions (28%). In addition, the NE cluster, which crossed over the Liaoning

734   Province and Tianjin, was dominated by SIA (25%), vehicle emissions (22%) and

735   coal combustion (20%). These results show that southern flows were dominant in

736   urban Beijing and were associated with higher SIA, vehicle emissions and coal

737   combustion contributions. Because SIA is primarily attributed to the transformation of

738   precursors that originate from oil and coal combustion (i.e., NO_x and SO_2), controlling

739   oil and coal combustion in the southern regions is required.

740   **4.4 Reconstructing the visibility**

741   In addition to particle size distributions, various chemical components play

742   significant but different roles in reducing visibility on haze days. To further

743   investigate the effects of the chemical species in the different size fractions and

744   meteorological factors on visibility, correlation analyses were performed and

745   regression model was used. SPSS 16.0 was used for multiple linear regression

746   analysis (Cheng et al., 2011).

747   In this study, 93 variables were investigated; however, only 7 variables were

748   selected because they had high correlation coefficients (> 0.5) with visibility. Overall,

749   the results (Table S3) showed that visibility had high correlation coefficients (> 0.5)

750   with SO_4^{2-} in the 0.43-0.65 μm and 0.65-1.1 μm size fractions, NH_4^+ in the 0.43-0.65

751   μm and NO_3^- in the 0.65-1.1 μm size fractions and Ca^{2+} in the 5.8-9 μm size fraction

752   as well as the RH and WS. All of the parameters that significantly affected visibility

753   were used as inputs in the multiple linear regression models to simulate visibility.

754   Ultimately, we developed the following regression equation for urban visibility in

755   Beijing (Line 756-757).

756   Visibility=$13.543-9.214RH+2.069WS-0.06[NH_4^+]_{0.43-0.65}-0.037[SO_4^{2-}]_{0.43-0.65}-0.44$

757 $5[SO_4^{2-}]_{0.65-1.1}-0.186[NO_3^-]_{0.65-1.1}-2.18[Ca^{2+}]_{5.8-9}$

758   Previously, SO_4^{2-}, NO_3^- and NH_4^+ in $PM_{2.5}$ were reported to play important roles

759 in visibility degradation during haze events in Beijing (Zhang et al., 2015). Compared

760 with previous studies, this study provides additional insights into the effects of

761 chemical species in different size fractions on the visibility.

762   In addition, the RH, WS and Ca^{2+} content are important for explaining changes in

763 visibility. High RH is conducive to the hygroscopic growth of particulate matter and

764 the generation of secondary species and reduces the visibility. In addition, Ca^{2+}

765 crucially affects visibility because it associated with dust, which strongly reduces

766 visibility. By contrast, high wind speeds are favorable for the diffusion of fine

767 particles and can improve visibility.

768   NH_4^+ in the 0.43-0.65 μm size fraction, SO_4^{2-} in the 0.65-1.1 μm size fraction, and

769 NO_3^- in the 0.65-1.1 μm size fraction are also among the most important factors that

770 affect visibility. These species primarily accumulated in the submicron particles.

771 Because the SO_4^{2-}, NO_3^- and NH_4^+ in this size fraction primarily originated from

772 gaseous precursors (NH_3, NO_2 and SO_2), regulations that control gaseous emissions of

773 these precursors are important for reducing PM pollution and therefore improving

774 visibility.

775   Our findings were similar to those reported for Jinan, in which the SO_4^{2-} and

776 water content in the 1.0-1.8 μm fraction and the RH were the most important factors

777 that affected visibility (Cheng et al., 2011). However, in this study, the Ca^{2+} in the

778 coarse particles, which primarily originated from construction dust and dust

779 transported over long distances (Liu et al., 2014a; Maenhaut et al., 2002b), also

780 played an important role in reducing the visibility in urban Beijing. However, the

781 transport of over long distances is not easy to control. Thus, we stress that

782 construction dust must be controlled to improve visibility.

783   To validate the above equation, datasets from other periods (from March 2012 to

784   February 2013) were used to characterize the relationships between visibility and

785   chemical species (Miao, 2014). As shown in Fig. S9, the estimated visibility was well

786   correlated with the measured visibility ($R^2 = 0.87$, $p < 0.05$). However, the ratio of the

787   estimated visibility to the measured visibility was only 0.78, and discrete points

788   primarily appeared for visibilities greater than 10 km (clear days). After scaling down,

789   i.e., using datasets with visibilities less than 10 km to validate the above equation, the

790   ratio of the estimated visibility to the measured visibility reached 1.15 and R^2 reached

791   0.97. This result indicated that the species that resulted in reduced visibility were

792   different for haze and clear conditions. This result is another indication that the above

793   equation can characterize the relationship between visibility and chemical species

794   during haze periods with a visibility of less than 10 km. This result will be useful for

795   reconstructing the relationships between visibility and particulate matter source and

796   we will do more discussion regarding this topic in the future.

797   **.5. Summary and conclusions**

798   The analysis of size-segregated airborne particles collected in Beijing from March

799   1, 2013 to February 28, 2014 was presented. The annual average mass concentrations

800   of the fine and coarse particles were higher than the National Ambient Air Quality

801   Standard (Grade I) of China. The OC, SO_4^{2-}, NO_3^- and NH_4^+ species were the most

802   abundant in the fine particles, accounting for 24.5%, 14.7%, 11.2% and 9.2% of the

803    $PM_{2.1}$ mass, respectively. In $PM_{2.1-9}$, the primary chemical components were Ca

804   (16.3%) and OC (15.5%). SOC, which formed due to photochemical reactions,

805   primarily accumulated in the "condensation mode". The size distribution of the OC

806   peaked at 0.43-0.65 μm in summer and at 0.65-1.1 μm in winter.

807   The dataset excluding extreme weather events (i.e., rain, snow, fog and dust) was

808   categorized into non-haze and haze days. NO_3^-, SO_4^{2-}, NH_4^+, Pb, Tl and Cd in $PM_{2.1}$

809   accumulated heavily during haze periods with $R_{H/N} > 2.6$. In coarse particles, the $R_{H/N}$

810   values of NH_4^+, NO_3^-, SO_4^{2-}, Cd, EC, Cl$^-$, Pb, Tl, Na$^+$, OC, Zn and K$^+$ were also

811 greater than unity, indicating that the effect of particles with a diameter larger than 2.1

812 μm cannot be neglected. The annual average size distributions of SO_4^{2-}, OC, NO_3^-,

813 NH_4^+, Cl^-, K^+ and Cd exhibited peak shifts from 0.43-0.65 μm on non-haze days to

814 0.65-1.1 μm on haze days. In addition, a regression equation was developed to

815 characterize the relationship between the visibility and the chemical species

816 concentrations when the visibility was less than 10 km.

817   The mass closure results showed that OM, SNA and CM dominated the fine and

818 coarse particulate mass concentrations. Although OM dominates in fine particles, it

819 decreased from 37.9% on non-haze days to 31.2% on haze days. In contrast, the

820 contribution of SNA to the $PM_{2.1}$ mass increased from 19.1% on non-haze days to

821 33.9% on haze days, indicating that SNA played a key role in haze formation.

822 Moreover, the SNA, OM, HM and EC contributions decreased as the size increased,

823 whereas those of CM and SS exhibited the opposite trend. Further studies are required

824 to determine the identities of the unidentified components in the larger size fractions.

825   Six $PM_{2.1}$ sources and seven $PM_{2.1-9}$ sources were identified using the PMF

826 method based on the annual size-segregated data. The source concentrations varied

827 between non-haze and haze days. The results show that coal combustion, vehicle

828 emissions, industrial pollution, biomass burning and secondary formation were major

829 contributors on haze days. In contrast, mineral dust (road dust) was important source

830 on non-haze days. In addition, the relative contributions of these sources in Beijing

831 varied significantly as the fraction sizes changed. The contributions of all of the

832 sources decreased as the size of the fraction increased with the exception of mineral

833 dust; however, they exhibited relatively high proportions in the fine and coarse modes,

834 indicating the importance of source apportionment for size sub-fractions within $PM_{2.1}$

835 and $PM_{2.1-9}$. Combining these findings with the trajectory clustering results, the source

836 regions associated with $PM_{2.1}$ in Beijing were further explored. We found that the

837 southern and northeastern flows are associated with greater SIA, vehicle emissions

838 and coal combustion contributions, whereas the northwestern flows transport more

839 mineral dust.

840 **Acknowledgements**

846 **References**

847 Bullock, K. R., Duvall, R. M., Norris, G. A., McDow, S. R., and Hays, M. D.:
848 Evaluation of the CMB and PMF models using organic molecular markers in fine
849 particulate matter collected during the Pittsburgh Air Quality Study, Atmos Environ,
850 42, 6897-6904, 2008.

851 Cao, J., Lee, S., Chow, J. C., Watson, J. G., Ho, K., Zhang, R., Jin, Z., Shen, Z., Chen,
852 G., and Kang, Y.: Spatial and seasonal distributions of carbonaceous aerosols over
853 China, J Geophys Res D, 112, doi:10.1029/2006JD008205, 2007.

854 Chan, C. Y., Xu, X. D., Li, Y. S., Wong, K. H., Ding, G. A., Chan, L. Y., and Cheng,
855 X. H.: Characteristics of vertical profiles and sources of $PM_{2.5}$, PM_{10} and
856 carbonaceous species in Beijing, Atmos Environ, 39, 5113-5124, 2005.

857 Cheng, S.-h., Yang, L.-x., Zhou, X.-h., Xue, L.-k., Gao, X.-m., Zhou, Y., and Wang,
858 W.-x.: Size-fractionated water-soluble ions, situ pH and water content in aerosol on
859 hazy days and the influences on visibility impairment in Jinan, China, Atmos Environ,
860 45, 4631-4640, 2011.

861 Cheng, Y., Engling, G., He, K. b., Duan, F. k., Du, Z. y., Ma, Y. l., Liang, L. l., Lu, Z.
862 f., Liu, J. m., Zheng, M., and Weber, R. J.: The characteristics of Beijing aerosol
863 during two distinct episodes: Impacts of biomass burning and fireworks, Environ
864 Pollut, 185, 149-157, 2014.

865 Contini, D., Cesari, D., Genga, A., Siciliano, M., Ielpo, P., Guascito, M. R., and Conte,
866 M.: Source apportionment of size-segregated atmospheric particles based on the major
867 water-soluble components in Lecce (Italy), Sci Total Environ, 472, 248-261, 2014.

868 Du, H., Kong, L., Cheng, T., Chen, J., Du, J., Li, L., Xia, X., Leng, C., and Huang, G.:
869 Insights into summertime haze pollution events over Shanghai based on online
870 water-soluble ionic composition of aerosols, Atmos Environ, 45, 5131-5137, 2011.

871 Du, Z., He, K., Cheng, Y., Duan, F., Ma, Y., Liu, J., Zhang, X., Zheng, M., and
872 Weber, R.: A year long study of water-soluble organic carbon in Beijing II: Light
873 absorption properties, Atmos Environ, 89, 235-241, 2014.

874 Duan, F., He, K., Ma, Y., Jia, Y., Yang, F., Lei, Y., Tanaka, S., and Okuta, T.:
875 Characteristics of carbonaceous aerosols in Beijing, China, Chemosphere, 60,
876 355-364, 2005.
877 Duarte, R. M. B. O., Mieiro, C. L., Penetra, A., Pio, C. A., and Duarte, A. C.:
878 Carbonaceous materials in size-segregated atmospheric aerosols from urban and
879 coastal-rural areas at the Western European Coast, Atmos Res, 90, 253-263, 2008.
880 Fisher, J. A., Jacob, D. J., Wang, Q., Bahreini, R., Carouge, C. C., Cubison, M. J.,
881 Dibb, J. E., Diehl, T., Jimenez, J. L., Leibensperger, E. M., Lu, Z., Meinders, M. B. J.,
882 Pye, H. O. T., Quinn, P. K., Sharma, S., Streets, D. G., van Donkelaar, A., and
883 Yantosca, R. M.: Sources, distribution, and acidity of sulfate–ammonium aerosol in
884 the Arctic in winter–spring, Atmos Environ, 45, 7301-7318, 2011.
885 Gao, J., Chai, F., Wang, T., Wang, S., and Wang, W.: Particle number size
886 distribution and new particle formation: New characteristics during the special
887 pollution control period in Beijing, J Environ Sci, 24, 14-21, 2012.
888 Guo, S., Hu, M., Wang, Z. B., Slanina, J., and Zhao, Y. L.: Size-resolved aerosol
889 water-soluble ionic compositions in the summer of Beijing: implication of regional
890 secondary formation, Atmos Chem Phys, 10, 947-959, 2010.
891 Guo, S., Hu, M., Zamora, M. L., Peng, J., Shang, D., Zheng, J., Du, Z., Wu, Z., Shao,
892 M., Zeng, L., Molina, M. J., and Zhang, R.: Elucidating severe urban haze formation
893 in China, Proceedings of the National Academy of Sciences of the United States of
894 America, 111, 17373-17378, 2014.
895 Hou, B., Zhuang, G., Zhang, R., Liu, T., Guo, Z., and Chen, Y.: The implication of
896 carbonaceous aerosol to the formation of haze: Revealed from the characteristics and
897 sources of OC/EC over a mega-city in China, J Hazard Mater, 190, 529-536, 2011.
898 Huang, R. J., Zhang, Y. L., Bozzetti, C., Ho, K. F., Cao, J. J., Han, Y. M.,
899 Daellenbach, K. R., Slowik, J. G., Platt, S. M., Canonaco, F., Zotter, P., Wolf, R.,
900 Pieber, S. M., Bruns, E. A., Crippa, M., Ciarelli, G., Piazzalunga, A., Schwikowski,
901 M., Abbaszade, G., Schnelle-Kreis, J., Zimmermann, R., An, Z. S., Szidat, S.,
902 Baltensperger, U., El Haddad, I., and Prevot, A. S. H.: High secondary aerosol
903 contribution to particulate pollution during haze events in China, Nature, 514,
904 218-222, 2014.
905 Hueglin, C., Gehrig, R., Baltensperger, U., Gysel, M., Monn, C., and Vonmont, H.:
906 Chemical characterisation of $PM_{2.5}$, PM_{10} and coarse particles at urban, near-city and
907 rural sites in Switzerland, Atmos Environ, 39, 637-651, 2005.
908 Jacobson, M. C., Hansson, H. C., Noone, K. J., and Charlson, R. J.: Organic
909 atmospheric aerosols: Review and state of the science, Rev Geophys, 38, 267-294,
910 2000.
911 Jing, H., Li, Y.-F., Zhao, J., Li, B., Sun, J., Chen, R., Gao, Y., and Chen, C.:
912 Wide-range particle characterization and elemental concentration in Beijing aerosol
913 during the 2013 Spring Festival, Environ Pollut, 192, 204-211, 2014.

Karanasiou, A. A., Siskos, P. A., and Eleftheriadis, K.: Assessment of source apportionment by Positive Matrix Factorization analysis on fine and coarse urban aerosol size fractions, Atmos Environ, 43, 3385-3395, 2009.

Karnae, S., and John, K.: Source apportionment of fine particulate matter measured in an industrialized coastal urban area of South Texas, Atmos Environ, 45, 3769-3776, 2011.

Li, X., Wang, L., Wang, Y., Wen, T., Yang, Y., Zhao, Y., and Wang, Y.: Chemical composition and size distribution of airborne particulate matters in Beijing during the 2008 Olympics, Atmos Environ, 50, 278-286, 2012a.

Li, X., Wang, L., Wang, Y., Wen, T., Yang, Y., Zhao, Y., and Wang, Y.: Chemical composition and size distribution of airborne particulate matters in Beijing during the 2008 Olympics, Atmos Environ, 50, 278-286, 2012b.

Li, X., Wang, L., Ji, D., Wen, T., Pan, Y., Sun, Y., and Wang, Y.: Characterization of the size-segregated water-soluble inorganic ions in the Jing-Jin-Ji urban agglomeration: Spatial/temporal variability, size distribution and sources, Atmos Environ, 77, 250-259, 2013.

Liu, Q., Liu, Y., Yin, J., Zhang, M., and Zhang, T.: Chemical characteristics and source apportionment of PM10 during Asian dust storm and non-dust storm days in Beijing, Atmos Environ, 91, 85-94, 2014a.

Liu, S., Hu, M., Slanina, S., He, L. Y., Niu, Y. W., Bruegemann, E., Gnauk, T., and Herrmann, H.: Size distribution and source analysis of ionic compositions of aerosols in polluted periods at Xinken in Pearl River Delta (PRD) of China, Atmos Environ, 42, 6284-6295, 2008.

Liu, Z. R., Hu, B., Liu, Q., Sun, Y., and Wang, Y. S.: Source apportionment of urban fine particle number concentration during summertime in Beijing, Atmos Environ, 2014b.

Maenhaut, W., Cafmeyer, J., Dubtsov, S., and Chi, X.: Detailed mass size distributions of elements and species, and aerosol chemical mass closure during fall 1999 at Gent, Belgium, Nuclear Instruments and Methods in Physics Research Section B: Beam Interactions with Materials and Atoms, 189, 238-242, 2002a.

Maenhaut, W., Schwarz, J., Cafmeyer, J., and Chi, X.: Aerosol chemical mass closure during the EUROTRAC-2 AEROSOL Intercomparison 2000, Nuclear Instruments and Methods in Physics Research Section B: Beam Interactions with Materials and Atoms, 189, 233-237, 2002b.

McFiggans, G.: ATMOSPHERIC SCIENCE Involatile particles from rapid oxidation, Nature, 506, 442-443, 2014.

Miao, H.: Spatial and temporal characterizations of water soluble inorganic ions of aerosol in China, Institute of Atmosphere Physics, Chinese Academy of Science, Beijing, 2014.

Moon, K. J., Han, J. S., Ghim, Y. S., and Kim, Y. J.: Source apportionment of fine carbonaceous particles by positive matrix factorization at Gosan background site in East Asia, Environ Int, 34, 654-664, 2008.

956 Paatero, P., and Tapper, U.: Positive matrix factorization: A non-negative factor
957 model with optimal utilization of error estimates of data values, Environmetrics, 5,
958 111-126, 1994.
959 Paatero, P.: Least square formulation of robust non-negative factor analysis,
960 Chemometr Intell Lab, 3, 23-35, 1997.
961 Pan, Y. P., Wang, Y. S., Tang, G. Q., and Wu, D.: Spatial distribution and temporal
962 variations of atmospheric sulfur deposition in Northern China: insights into the
963 potential acidification risks, Atmos Chem Phys, 13, 1675-1688, 2013.
964 Pan, Y. P., and Wang, Y. S.: Atmospheric wet and dry deposition of trace elements at
965 10 sites in Northern China, Atmos Chem Phys, 15, 951-972, 2015.
966 Pant, P., and Harrison, R. M.: Critical review of receptor modelling for particulate
967 matter: A case study of India, Atmos Environ, 49, 1-12, 2012.
968 Pillai, P. S., and Moorthy, K. K.: Aerosol mass-size distributions at a tropical coastal
969 environment: response to mesoscale and synoptic processes, Atmos Environ, 35,
970 4099-4112, 2001.
971 Quan, J., Tie, X., Zhang, Q., Liu, Q., Li, X., Gao, Y., and Zhao, D.: Characteristics of
972 heavy aerosol pollution during the 2012-2013 winter in Beijing, China, Atmos
973 Environ, 88, 83-89, 2014.
974 Schleicher, N., Norra, S., Fricker, M., Kaminski, U., Chen, Y., Chai, F., Wang, S., Yu,
975 Y., and Cen, K.: Spatio-temporal variations of black carbon concentrations in the
976 Megacity Beijing, Environ Pollut, 182, 392-401, 2013.
977 Sirois, A., and Bottenheim, J. W.: Use of backward trajectories to interpret the 5-year
978 record of PAN and O_3 ambient air concentrations at Kejimkujik National Park, Nova
979 Scotia, J Geophys Res D, 100, 2867-2881, 1995.
980 Song, Y., Zhang, Y., Xie, S., Zeng, L., Zheng, M., Salmon, L. G., Shao, M., and
981 Slanina, S.: Source apportionment of $PM_{2.5}$ in Beijing by positive matrix factorization,
982 Atmos Environ, 40, 1526-1537, 2006.
983 Song, Y., Tang, X., Xie, S., Zhang, Y., Wei, Y., Zhang, M., Zeng, L., and Lu, S.:
984 Source apportionment of PM2.5 in Beijing in 2004, J Hazard Mater, 146, 124-130,
985 2007.
986 Streets, D. G., Fu, J. S., Jang, C. J., Hao, J., He, K., Tang, X., Zhang, Y., Wang, Z., Li,
987 Z., Zhang, Q., Wang, L., Wang, B., and Yu, C.: Air quality during the 2008 Beijing
988 Olympic Games, Atmos Environ, 41, 480-492, 2007.
989 Sun, J., Zhang, Q., Canagaratna, M. R., Zhang, Y., Ng, N. L., Sun, Y., Jayne, J. T.,
990 Zhang, X., Zhang, X., and Worsnop, D. R.: Highly time- and size-resolved
991 characterization of submicron aerosol particles in Beijing using an Aerodyne Aerosol
992 Mass Spectrometer, Atmos Environ, 44, 131-140, 2010.
993 Sun, Y., Zhuang, G., Wang, Y., Han, L., Guo, J., Dan, M., Zhang, W., Wang, Z., and
994 Hao, Z.: The air-borne particulate pollution in Beijing—concentration, composition,
995 distribution and sources, Atmos Environ, 38, 5991-6004, 2004.

996 Sun, Y., Zhuang, G., Tang, A., Wang, Y., and An, Z.: Chemical characteristics of
997 $PM_{2.5}$ and PM_{10} in haze-fog episodes in Beijing, Environ Sci Technol, 40, 3148-3155,
998 2006.

999 Sun, Z., Mu, Y., Liu, Y., and Shao, L.: A comparison study on airborne particles
1000 during haze days and non-haze days in Beijing, Sci Total Environ, 456–457, 1-8,
1001 2013.

1002 Tan, J. H., Duan, J. C., Chen, D. H., Wang, X. H., Guo, S. J., Bi, X. H., Sheng, G. Y.,
1003 He, K. B., and Fu, J. M.: Chemical characteristics of haze during summer and winter
1004 in Guangzhou, Atmos Res, 94, 238-245, 2009.

1005 Tian, S., Pan, Y., Liu, Z., Wen, T., and Wang, Y.: Size-resolved aerosol chemical
1006 analysis of extreme haze pollution events during early 2013 in urban Beijing, China, J
1007 Hazard Mater, 279, 452-460, 2014.

1008 Titos, G., Lyamani, H., Pandolfi, M., Alastuey, A., and Alados-Arboledas, L.:
1009 Identification of fine (PM_1) and coarse (PM_{10-1}) sources of particulate matter in an
1010 urban environment, Atmos Environ, 89, 593-602, 2014.

1011 Vecchi, R., Chiari, M., D'Alessandro, A., Fermo, P., Lucarelli, F., Mazzei, F., Nava,
1012 S., Piazzalunga, A., Prati, P., Silvani, F., and Valli, G.: A mass closure and PMF
1013 source apportionment study on the sub-micron sized aerosol fraction at urban sites in
1014 Italy, Atmos Environ, 42, 2240-2253, 2008.

1015 Wang, G., Kawamura, K., Lee, S., Ho, K., and Cao, J.: Molecular, Seasonal, and
1016 Spatial Distributions of Organic Aerosols from Fourteen Chinese Cities, Environ Sci
1017 Technol, 40, 4619-4625, 2006a.

1018 Wang, L., Xin, J., Li, X., and Wang, Y.: The variability of biomass burning and its
1019 influence on regional aerosol properties during the wheat harvest season in North
1020 China, Atmos Res, 157, 153-163, 2015.

1021 Wang, L. T., Wei, Z., Yang, J., Zhang, Y., Zhang, F. F., Su, J., Meng, C. C., and
1022 Zhang, Q.: The 2013 severe haze over southern Hebei, China: model evaluation,
1023 source apportionment, and policy implications, Atmos Chem Phys, 14, 3151-3173,
1024 2014.

1025 Wang, X., Wang, W., Yang, L., Gao, X., Nie, W., Yu, Y., Xu, P., Zhou, Y., and Wang,
1026 Z.: The secondary formation of inorganic aerosols in the droplet mode through
1027 heterogeneous aqueous reactions under haze conditions, Atmos Environ, 63, 68-76,
1028 2012.

1029 Wang, Y. Q., Zhang, X. Y., and Arimoto, R.: The contribution from distant dust
1030 sources to the atmospheric particulate matter loadings at XiAn, China during spring,
1031 Sci Total Environ, 368, 875-883, 2006b.

1032 Yan, C., Zheng, M., Sullivan, A. P., Bosch, C., Desyaterik, Y., Andersson, A., Li, X.,
1033 Guo, X., Zhou, T., Gustafsson, Ö., and Collett Jr, J. L.: Chemical characteristics and
1034 light-absorbing property of water-soluble organic carbon in Beijing: Biomass burning
1035 contributions, Atmos Environ, 2015.

Yang, L., Cheng, S., Wang, X., Nie, W., Xu, P., Gao, X., Yuan, C., and Wang, W.: Source identification and health impact of PM$_{2.5}$ in a heavily polluted urban atmosphere in China, Atmos Environ, 75, 265-269, 2013.

Yang, X., Chen, Y. Z., Liu, H. F., Zhao, Y. X., Gao, J., Chai, F. H., and Meng, F.: Characteristics and formation mechanism of a serious haze event in January 2013 in Beijing, China Environ Sci, 34, 282-288, 2014.

Yang, Y., Wang, Y., Wen, T., Wei, L., Ya'nan, Z., and Liang, L.: Elemental composition of PM2.5 and PM10 at Mount Gongga in China during 2006, Atmos Res, 93, 801-810, 2009.

Yao, X., Lau, A. P. S., Fang, M., Chan, C. K., and Hu, M.: Size distributions and formation of ionic species in atmospheric particulate pollutants in Beijing, China: inorganic ions, Atmos Environ, 37, 2991-3000, 2003.

Zhang, G., Bi, X., Chan, L. Y., Wang, X., Sheng, G., and Fu, J.: Size-segregated chemical characteristics of aerosol during haze in an urban area of the Pearl River Delta region, China, Urban Clim, 4, 74-84, 2013a.

Zhang, H., Hu, J., Kleeman, M., and Ying, Q.: Source apportionment of sulfate and nitrate particulate matter in the Eastern United States and effectiveness of emission control programs, Sci Total Environ, 490, 171-181, 2014a.

Zhang, J. K., Sun, Y., Liu, Z. R., Ji, D. S., Hu, B., Liu, Q., and Wang, Y. S.: Characterization of submicron aerosols during a month of serious pollution in Beijing, 2013, Atmos Chem Phys, 14, 2887-2903, 2014b.

Zhang, Q., Quan, J., Tie, X., Li, X., Liu, Q., Gao, Y., and Zhao, D.: Effects of meteorology and secondary particle formation on visibility during heavy haze events in Beijing, China, Sci Total Environ, 502, 578-584, 2015.

Zhang, R., Jing, J., Tao, J., Hsu, S. C., Wang, G., Cao, J., Lee, C. S. L., Zhu, L., Chen, Z., Zhao, Y., and Shen, Z.: Chemical characterization and source apportionment of PM$_{2.5}$ in Beijing: seasonal perspective, Atmos Chem Phys, 13, 7053-7074, 2013b.

Zhang, W., Zhuang, G., Guo, J., Xu, D., Wang, W., Baumgardner, D., Wu, Z., and Yang, W.: Sources of aerosol as determined from elemental composition and size distributions in Beijing, Atmos Res, 95, 197-209, 2010.

Zhang, X. Y., Wang, Y. Q., Zhang, X. C., Guo, W., and Gong, S. L.: Carbonaceous aerosol composition over various regions of China during 2006, J Geophys Res D, 113, D14111, 2008.

Zheng, M., Salmon, L. G., Schauer, J. J., Zeng, L., Kiang, C. S., Zhang, Y., and Cass, G. R.: Seasonal trends in PM2.5 source contributions in Beijing, China, Atmos Environ, 39, 3967-3976, 2005.

Zhuang, X., Wang, Y., He, H., Liu, J., Wang, X., Zhu, T., Ge, M., Zhou, J., Tang, G., and Ma, J.: Haze insights and mitigation in China: An overview, J Environ Sci, 26, 2-12, 2014.
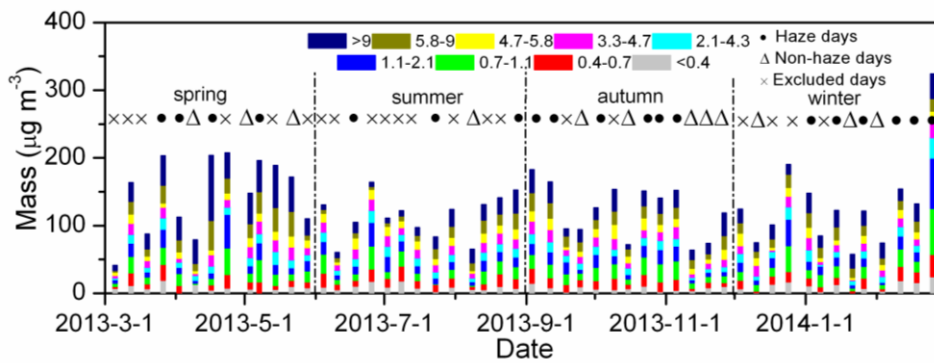
1096

1097

1098 Fig. 1 Mass concentration size distributions and that of typical chemical species in
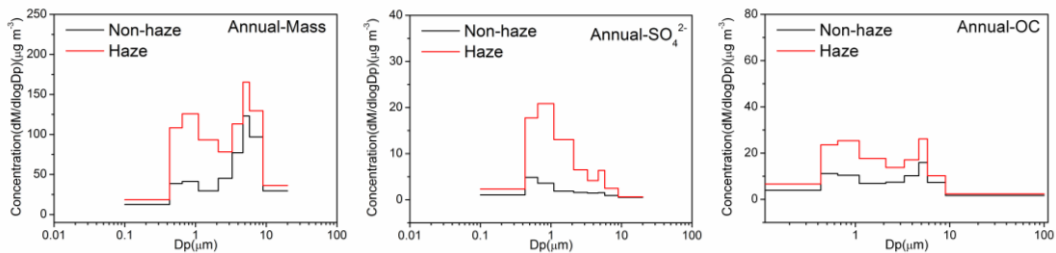
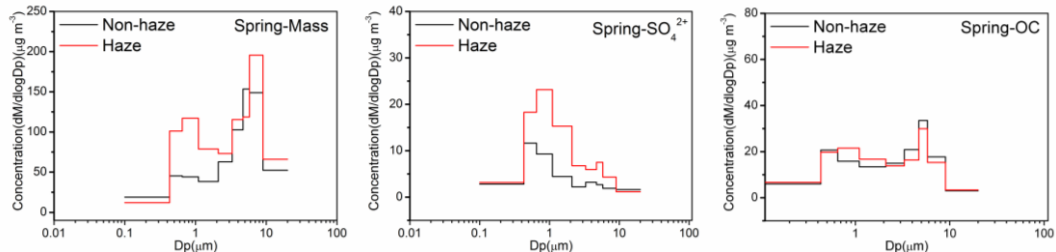1099 different categories.

1100

1101

1102 Figure 2. Size-resolved mass concentration (distributions that are marked as solid

1103 circle and open triangle denote haze and non-haze days, respectively).
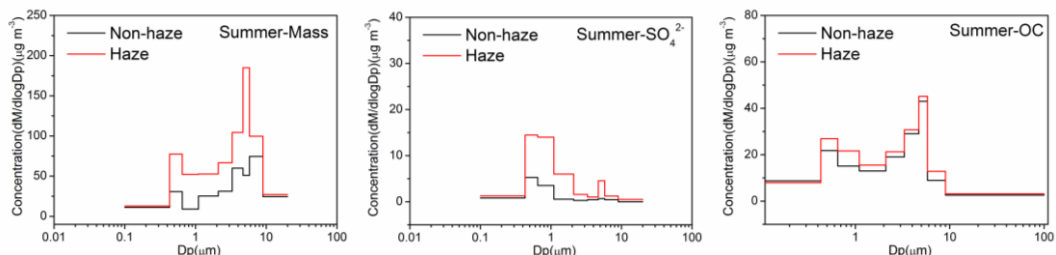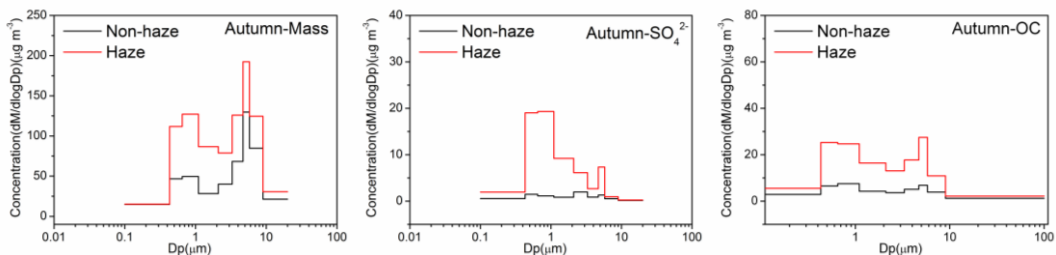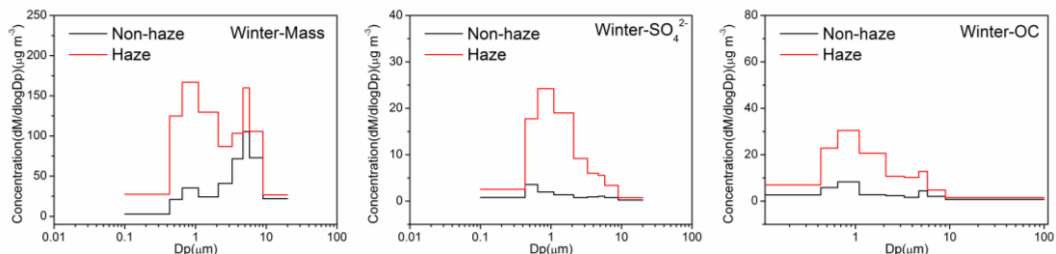
1104

Figure 3. Mass concentration size distributions on haze and non-haze days over the entire sampling period (annual) and by season as well as that of the typical chemical species.
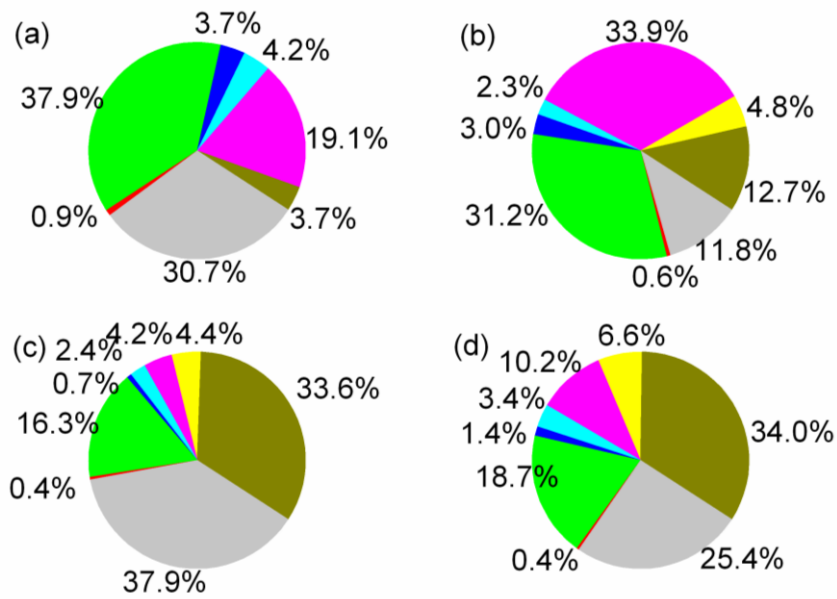
1114
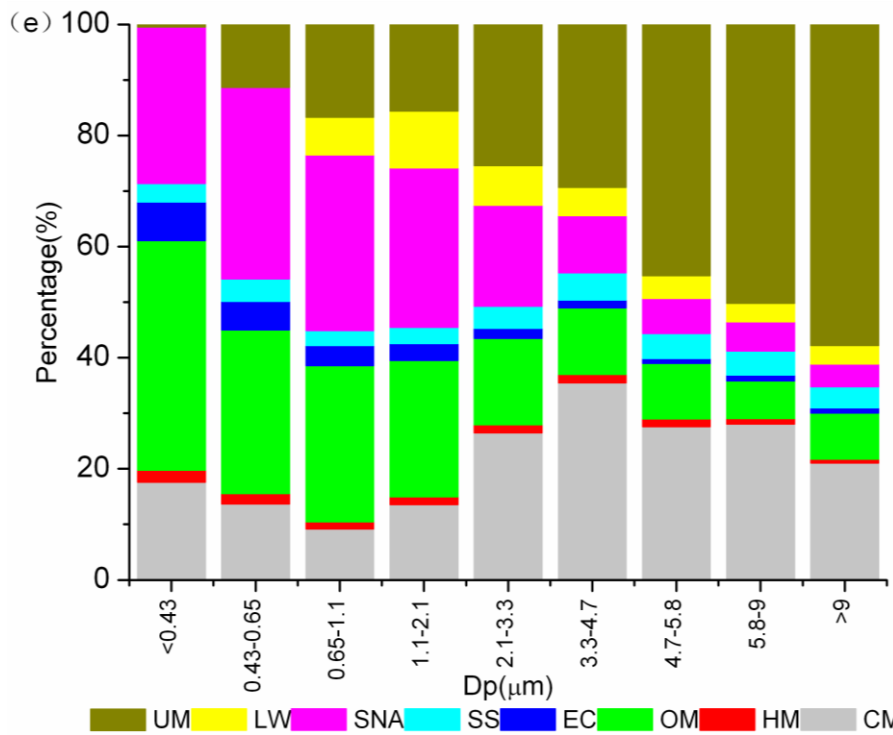
1115

Fig. 4 Contributions of different components to the total masses in (a) $PM_{2.1}$ on

non-haze days; (b) $PM_{2.1}$ on haze days; (c) $PM_{2.1-9}$ on non-haze days; (d) $PM_{2.1-9}$ on

haze days; (e) different size fractions.

1120
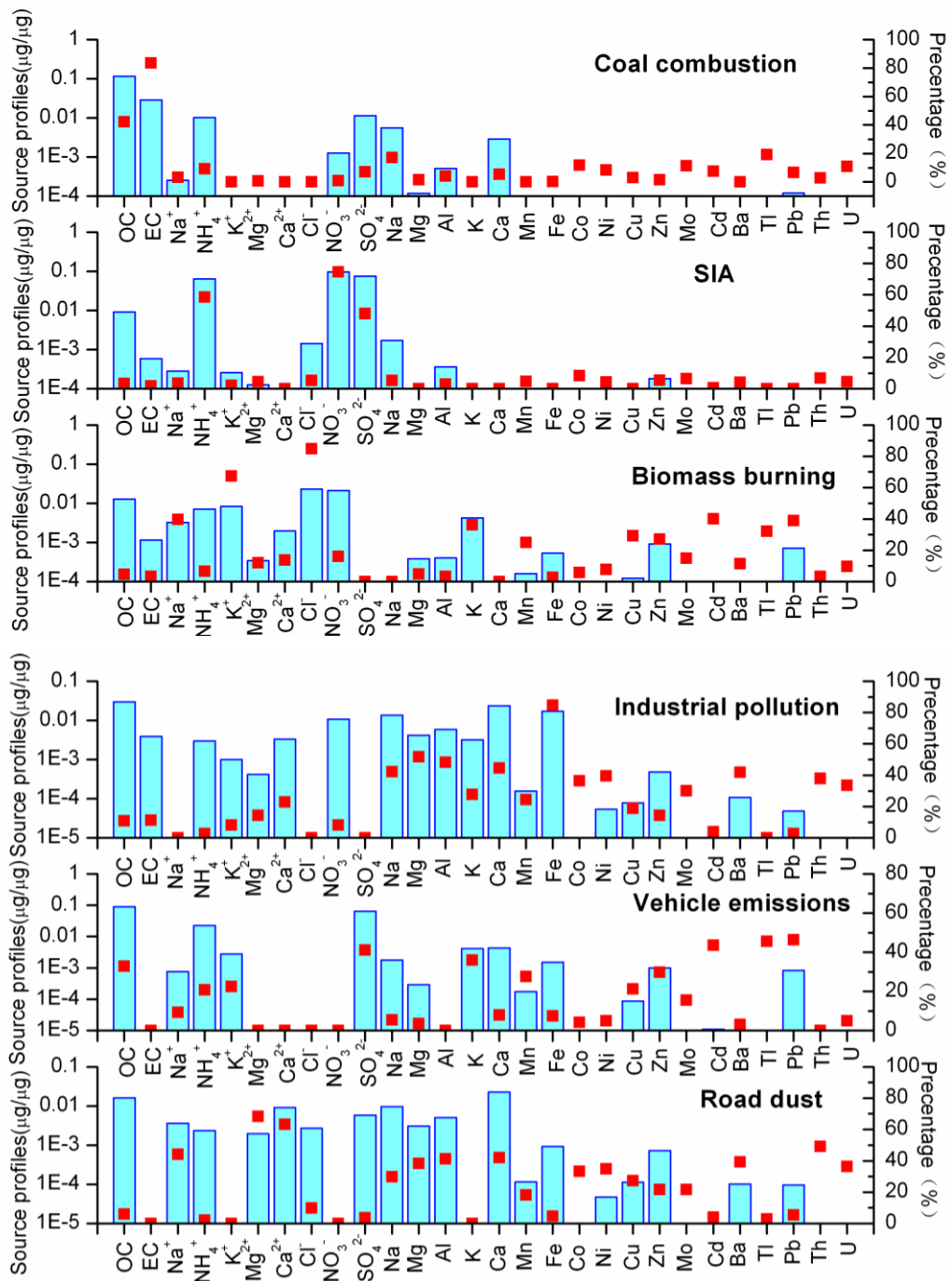
1121
1122

(a)

1123
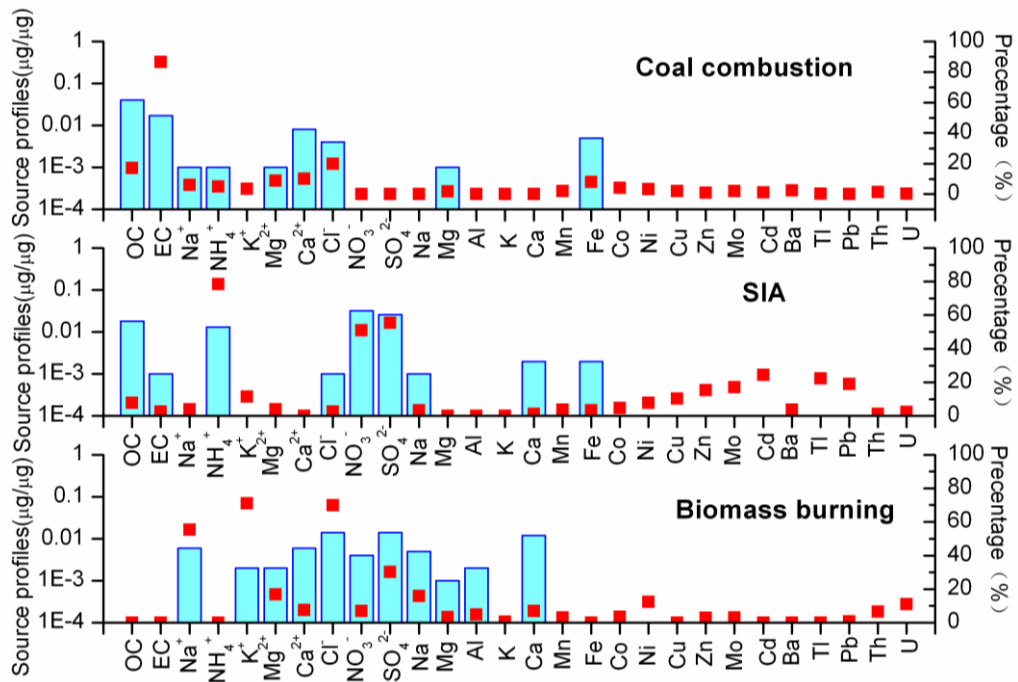
1124
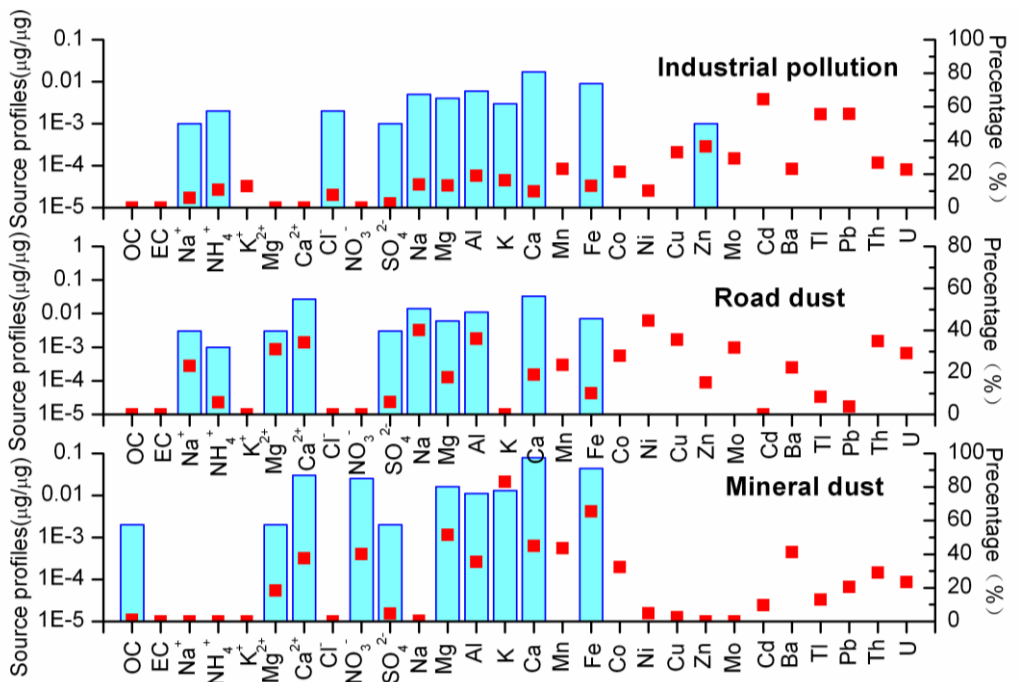
1125
1126   (b)

1127   Figure 5. The profiles of each source in (a) fine and (b) coarse fractions.

1128
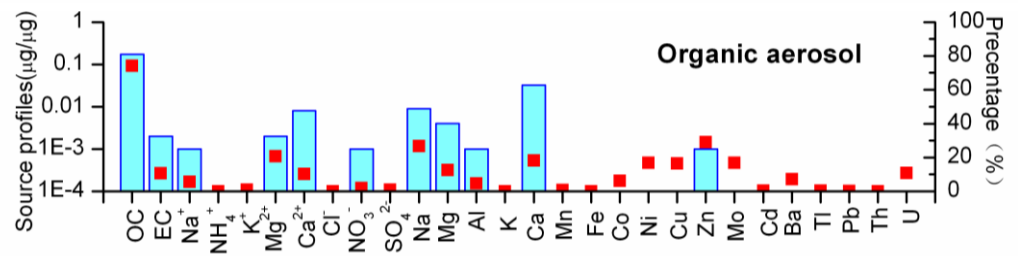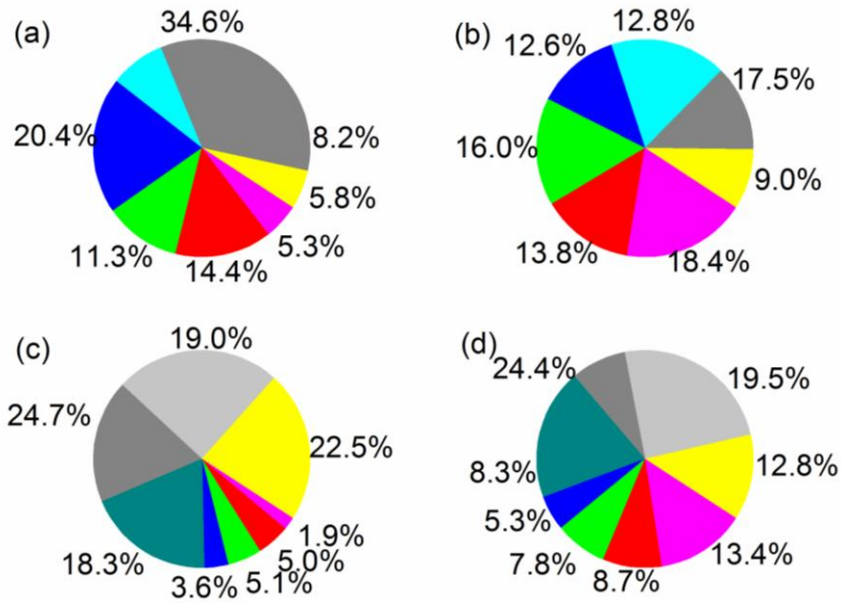
1129
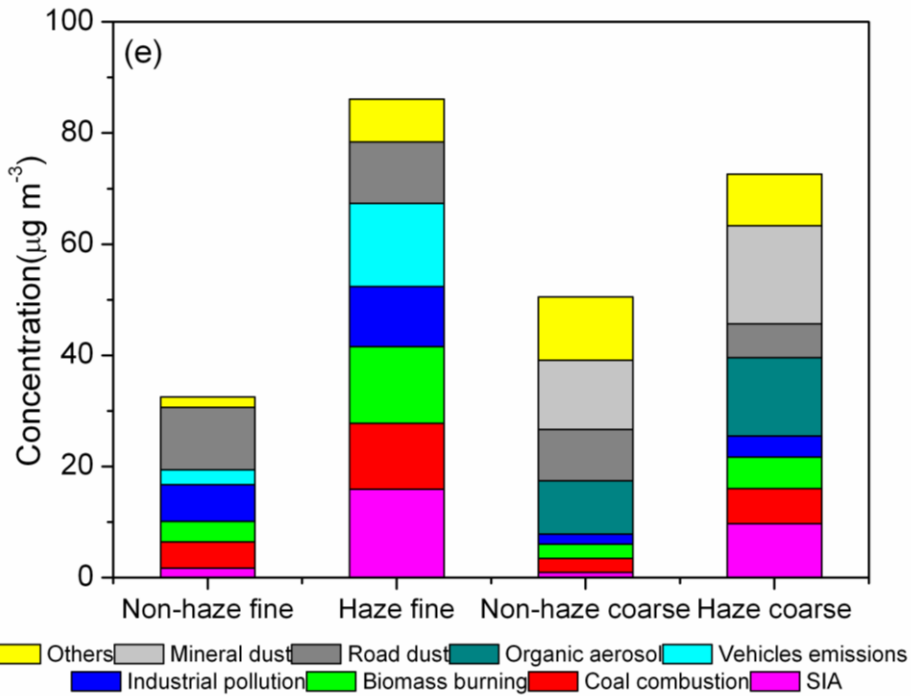
1130

Figure 6. Relative contributions from each identified source to (a) PM$_{2.1}$ on non-haze
days; (b) PM$_{2.1}$ on haze days; (c) PM$_{2.1-9}$ on non-haze days; (d) PM$_{2.1-9}$ on haze days
and (e) mass concentrations of each source.

1135
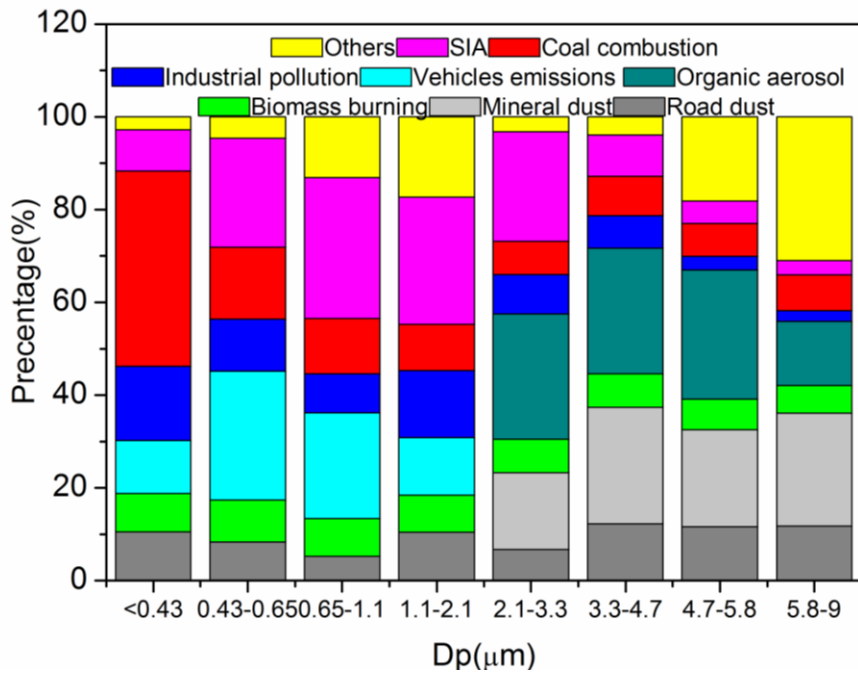
1136   Figure 7. Relative contributions from each identified source to different size fractions.

1137
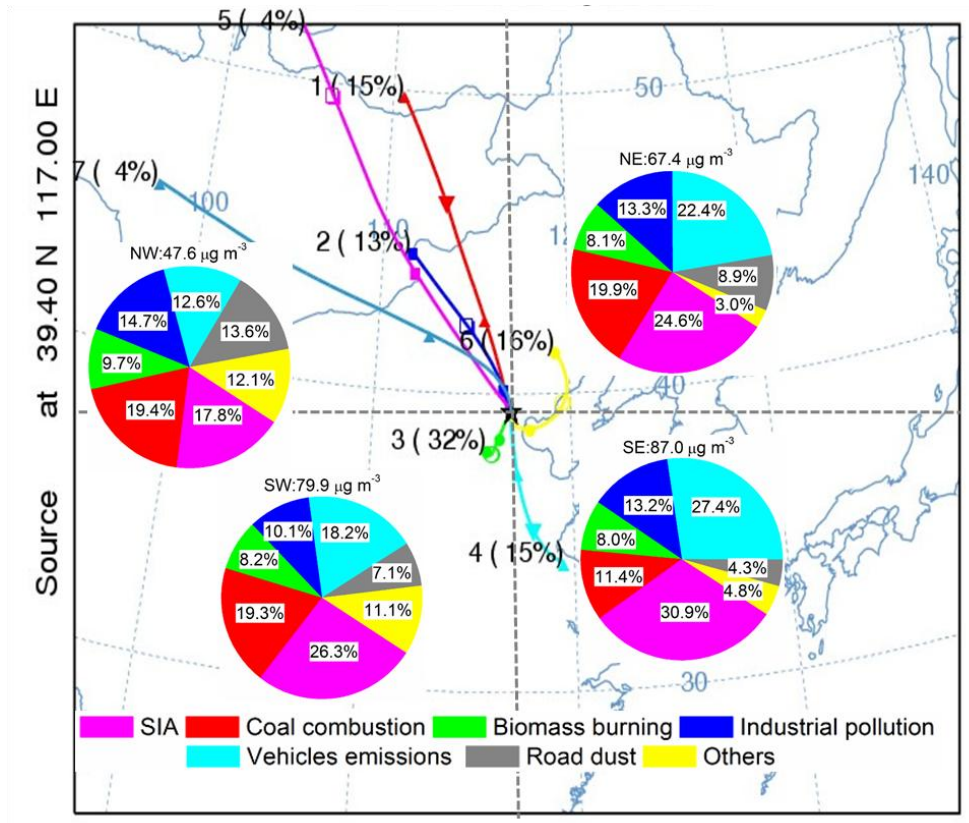
1138

1139   Figure 8. Relative contributions from each identified source to PM$_{2.1}$ at different

1140   trajectory clusters.

1141 Table 1 Concentrations of different chemical compositions in size-resolved particles during entire sampling period (annual) and four seasons (µg

1142 m^{-3}).

Size	Annual		Spring		Summer		Autumn		Winter	
	$PM_{2.1}$	$PM_{2.1-9}$	$PM_{2.1}$	$PM_{2.1-9}$	$PM_{2.1}$	$PM_{2.1-9}$	$PM_{2.1}$	$PM_{2.1-9}$	$PM_{2.1}$	$PM_{2.1-9}$
Mass	67.27	62.33	64.65	68.05	65.05	57.97	62.52	62.87	76.84	60.41
OC	16.50	9.63	16.26	10.44	20.19	16.68	13.40	6.76	16.16	4.64
EC	2.01	0.77	1.28	0.71	1.47	0.81	1.99	0.82	3.32	0.75
Na^+	0.79	0.66	0.48	0.57	0.27	0.31	1.67	0.92	0.74	0.82
NH_4^+	6.17	0.70	8.00	0.74	6.11	0.41	4.65	0.56	5.92	1.08
K^+	0.72	0.29	0.83	0.49	0.33	0.12	0.60	0.09	1.12	0.46
Mg^{2+}	0.21	0.40	0.30	0.41	0.14	0.36	0.20	0.42	0.20	0.40
Ca^{2+}	1.01	3.38	1.25	3.98	0.67	2.69	1.00	3.77	1.10	3.08
Cl^-	1.58	0.81	1.98	1.19	0.17	0.31	1.23	0.46	2.95	1.28
NO_3^-	7.51	2.78	8.51	3.56	4.08	2.33	6.60	2.46	10.84	2.76
SO_4^{2-}	9.87	2.17	11.02	2.80	10.02	1.47	9.28	2.08	9.16	2.35
Na	1.78	1.34	1.77	1.33	1.81	1.12	1.81	1.29	1.73	1.64
Mg	0.45	1.19	0.51	1.63	0.49	1.08	0.46	1.14	0.35	0.91
Al	0.65	1.39	0.73	2.06	0.60	0.90	0.69	1.32	0.59	1.29
K	0.69	0.62	0.88	0.98	0.49	0.49	0.74	0.59	0.65	0.42
Ca	3.54	10.17	4.03	16.31	4.63	10.20	3.21	8.63	2.30	5.55
Mn	0.04	0.04	0.05	0.06	0.03	0.03	0.04	0.04	0.03	0.04
Fe	1.23	2.58	1.55	3.66	1.43	2.08	1.36	2.62	0.58	1.98
Co	0.001	0.001	0.001	0.001	0.001	0.001	0.001	0.001	0.001	0.001

Ni	0.013	0.014	0.011	0.012	0.014	0.010	0.014	0.018	0.014	0.015
Cu	0.026	0.020	0.030	0.020	0.015	0.015	0.029	0.022	0.029	0.023
Zn	0.21	0.10	0.24	0.12	0.18	0.09	0.23	0.09	0.19	0.09
Mo	0.006	0.006	0.002	0.001	0.002	0.002	0.002	0.001	0.002	0.002
Cd	0.001	0.000	0.001	0.000	0.001	0.000	0.001	0.000	0.001	0.000
Ba	0.017	0.043	0.018	0.057	0.014	0.032	0.018	0.044	0.017	0.039
Tl	0.001	0.000	0.001	0.000	0.001	0.000	0.001	0.000	0.001	0.000
Pb	0.089	0.018	0.094	0.022	0.071	0.013	0.088	0.015	0.103	0.022
Th	0.000	0.000	0.000	0.001	0.000	0.000	0.000	0.000	0.000	0.001
U	0.000	0.000	0.000	0.000	0.000	0.000	0.000	0.000	0.000	0.000

1143

1144

1145